

Supporting Information

Exciton coupling chirality in helicene-porphyrin conjugates

Kais Dhbaibi,^a Paola Matozzo,^a Laura Abella,^b Marion Jean,^c Nicolas Vanthuyne,^c Jochen Autschbach,^{*b} Ludovic Favereau,^{*a} and Jeanne Crassous^{*a}

a. Univ Rennes, CNRS, ISCR-UMR 6226, ScanMAT-UMS 2001, F-35000 Rennes, France.
Emails: ludovic.favereau@univ-rennes1.fr; jeanne.crassous@univ-rennes1.fr

b. Department of Chemistry, University at Buffalo, State University of New York, Buffalo, NY 14260, USA.
E-mail: jochena@buffalo.edu

c. Aix Marseille University, CNRS Centrale Marseille, iSm2, 13284 Marseille, France.

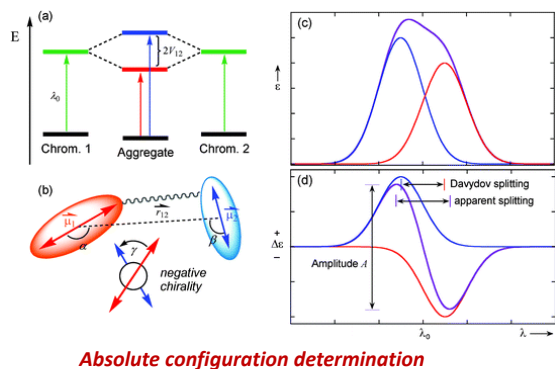
Table of Contents

I. Principle of exciton coupling chirality	S2
II. Experimental procedure	
A. General method.....	S2
B. Synthetic procedures.....	S3
C. NMR spectra.....	S7
D. MALDI-TOF spectra.....	S15
E. Photophysical characterization.....	S17
III. Computational part.....	S22
IV. References.....	S39

I. Principle of Exciton Coupling Chirality

Chromophores with strong electric dipolar moments can be grafted at each extremity of a helical and generate Exciton Coupling Chirality, giving a typical bisignate signature in the CD (negative-positive or positive-negative, depending on the chirality).¹

a) Principle of exciton coupling chirality



b) Exciton coupling in chiral bis-porphyrins

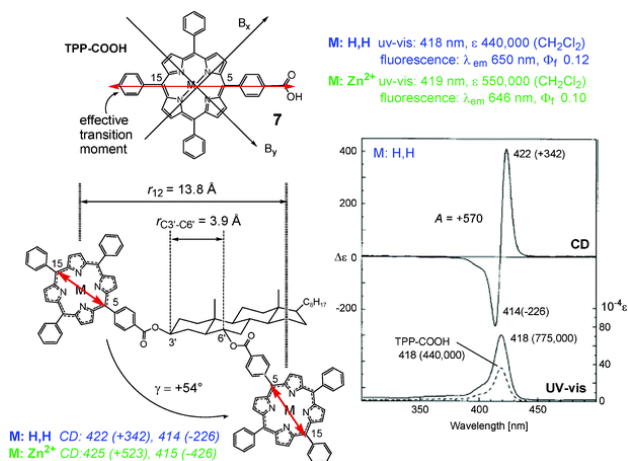


Figure S1.1. Exciton coupling chirality and its application in diol substituted with porphyrins.

II. Experimental procedures

A. General method

¹H and ¹³C NMR spectra were recorded at room temperature on an *AVANCE III 400 BRUKER* or an *AVANCE I 500 BRUKER* at Centre Régional de Mesures Physiques de l'Ouest (CRMPO), Université de Rennes 1. Chemical shifts δ are given in ppm and coupling constants J in Hz. Chemical shifts for ¹H NMR spectra are referenced relative to residual protium in the deuterated solvent ($\delta = 7.26$ ppm, CDCl₃, $\delta = 5.32$ ppm, CD₂Cl₂). ¹³C shifts are referenced to deuterated solvent ($\delta = 77.2$ ppm for CDCl₃, $\delta = 53.8$ ppm, CD₂Cl₂).

High-resolution mass (HR-MS) determinations were performed at CRMPO on a Bruker MaXis 4G by ASAP (+ or -) or ESI with CH₂Cl₂ as solvent techniques. Experimental and calculated masses are given with consideration of the mass of the electron.

UV-Visible (UV-vis, in M⁻¹ cm⁻¹) absorption spectra were recorded on a UV-2401PC Shimadzu spectrophotometer. Fluorescence spectra were recorded on a FL 920 Edinburgh fluorimeter.

Electronic circular dichroism (ECD, in M⁻¹ cm⁻¹) was measured on a Jasco J-815 Circular Dichroism Spectrometer (IFR140 facility - Biosit - Université de Rennes 1).

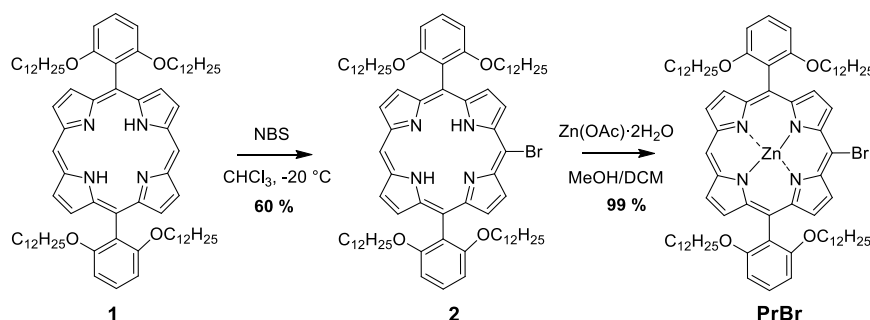
The circularly polarized luminescence (CPL) measurements of compound **H6Pr2** were performed using a home-built CPL spectrofluoropolarimeter (constructed with the help of the JASCO Company). The samples were excited using a 90° geometry with a Xenon ozone-free lamp 150 W LS. The following parameters were used: emission slit width \approx 10 mm, integration time = 8 sec, scan speed = 50 nm/min, accumulations = 5. The concentration of all the samples was ca. 10^{-6} M. Excitation of the samples was performed at 446 nm. CPL of compound **H6Pr3** was also performed using a commercial CPL-300 spectrofluoropolarimeter at JASCO Europe (Cremella, Italy). The samples were excited using a 180° geometry with a Xenon ozone-free lamp 150 W LS and by using the same parameters as described above.

Thin-layer chromatography (TLC) was performed on aluminum sheets precoated with Merck 5735 Kieselgel 60F254. Column chromatography was carried out with Merck 5735 Kieselgel 60F (0.040-0.063 mm mesh).

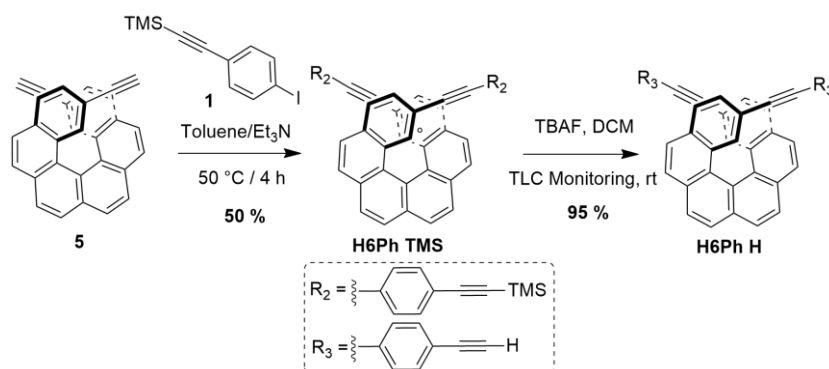
Chemicals were purchased from Sigma-Aldrich, Alfa Aesar or TCI Europe, and used as received.

B. Synthetic procedures

((4-Iodophenyl)ethynyl)trimethylsilane and compound **1** were purchased from fluorochem. Compounds **2** and **PrBr** were prepared according to the scheme S1.1 and following the procedure described in the literature.^{2,3} *P*- and *M*-**5** enantiomers were obtained following a strategy previously reported by our group.⁴



Scheme S1.1. Preparation of porphyrin synthons



Scheme S1.2. Preparation of helicene synthons

chromatography (100 % CH₂Cl₂) to give the final product as yellow solid (38 mg, 95 %). *M*-**H6PhH** (38 mg, 95 %) was obtained from *M*-**H6PhTMS** (50 mg, 0.07 mmol) under identical conditions.

¹H NMR (400 MHz, Methylene Chloride-d₂) δ 8.15 – 7.98 (m, 8H), 7.87 (d, J = 8.2 Hz, 2H), 7.82 (d, J = 1.5 Hz, 2H), 7.52 – 7.47 (m, 4H), 7.41 (dd, J = 8.3, 1.6 Hz, 2H), 7.36 – 7.30 (m, 4H), 3.29 (s, 2H).

¹³C NMR (101 MHz, Methylene Chloride-d₂) δ 133.4, 132, 131.9, 131.8, 131.8, 131.2, 129.1, 127.8, 127.7, 127.5, 127.4, 127, 123.8, 121.6, 119, 91.6, 88.1, 83, 78.8.

P-**H6Pr1** and (*P,P*)-**H6Pr2** (and their *M* configured enantiomers)

A mixture of compound *P*-**H6PhH** (10 mg, 0.017 mmol), **PrBr** (51 mg, 0.038 mmol), CuI (0.6 mg, 0.0034 mmol), and Pd (PPh₃)₄ (2 mg, 0.0017 mmol) in Toluene (4 mL) and NEt₃ (1 mL) was stirred and heated at 60°C under argon atmosphere for 12 h. After removal of the solvent, the residue was dissolved again in CH₂Cl₂. The organic phase was washed with water and dried over anhydrous Na₂SO₄. The solvent was removed under vacuum, and the crude product was purified by column chromatography using CH₂Cl₂/ Ethylacetate (8:2) as the eluent to furnish the expected helicene porphyrin derivatives *P*-**H6Pr1** (10 mg, 19 %) with a side product (*P,P*)-**H6Pr2** respectively, as a green solid (10 mg, 16 %). The *M* configured enantiomers *M*-**H6Pr1** (9.5 mg, 18 %) and (*M,M*)-**H6Pr2** (10.6 mg, 17 %) were obtained from *M*-**H6PhH** (10 mg, 0.017 mmol) under identical conditions.

H6Pr1

¹H NMR (400 MHz, Methylene Chloride-d₂) δ 10.15 (s, 2H), 9.85 (d, J = 4.6 Hz, 4H), 9.32 (d, J = 4.4 Hz, 4H), 9.02 (dd, J = 24.6, 4.5 Hz, 8H), 8.21 – 8.13 (m, 8H), 8.11 – 7.93 (m, 8H), 7.79 (t, J = 8.4 Hz, 4H), 7.63 – 7.52 (m, 6H), 7.11 (d, J = 8.5 Hz, 8H), 3.93 (t, J = 6.4 Hz, 16H), 1.35 – 1.08 (m, 40H), 1.06 – 0.84 (m, 71H), 0.72 (p, J = 7.2 Hz, 17H), 0.62 – 0.46 (m, 36H), 0.40 (p, J = 7.7 Hz, 17H).

¹³C NMR (101 MHz, Methylene Chloride-d₂) δ 159.9, 151.4, 151, 150.2, 149.3, 132.1, 131.6, 131.3, 130.3, 129.9, 128, 127.5, 127.2, 124.3, 120.6, 119.4, 114.2, 106.6, 105.2, 98.6, 91.5, 88.8, 68.6, 31.9, 29.7, 29.4(d, J = 7.5 Hz), 29.2(d, J = 5.7 Hz), 29.1, 28.6(d, J = 3.1 Hz), 25.2, 22.7, 13.9, 0.7.

HR-MS Ultraflex III, MALDI, 370 °C; ion [M]⁺, C₂₀₆ H₂₅₂ N₈ O₈ ⁶⁴Zn₂, m/z calculated 3093.81356, m/z experimental 3093.780 (Δ=11 ppm).

H6Pr2

¹H NMR (400 MHz, Methylene Chloride-d₂) δ 10.14 (s, 2H), 9.84 (d, $J = 4.6$ Hz, 4H), 9.31 (d, $J = 4.5$ Hz, 4H), 9.01 (dd, $J = 23.7, 4.5$ Hz, 8H), 8.23 – 8.03 (m, 22H), 8.02 – 7.88 (m, 8H), 7.79 (t, $J = 8.4$ Hz, 4H), 7.58 (d, $J = 8.2$ Hz, 8H), 7.54 – 7.48 (m, 4H), 7.39 (d, $J = 8.2$ Hz, 4H), 7.10 (d, $J = 8.5$ Hz, 8H), 3.93 (t, $J = 6.4$ Hz, 16H), 1.33 – 1.06 (m, 40H), 1.06 – 0.84 (m, 80H), 0.71 (p, $J = 7.2$ Hz, 16H), 0.61 – 0.47 (m, 36H), 0.46 – 0.35 (m, 16H).

¹³C NMR (101 MHz, Methylene Chloride-d₂) δ 167.5, 159.9, 151.4, 151, 150.2, 149.2, 132.4, 132.5, 132.1, 131.9, 131.5, 131.4, 131.3, 130.9, 129.8, 128.7, 127.5, 120.6, 114.2, 105.2, 68.6, 67.9, 53.4(p, $J = 27.1$ Hz), 38.8, 31.9, 30.4, 29.7, 29.5, 29.4, 29.3, 29.2, 29.1, 28.6(d, $J = 2.7$ Hz), 25.2, 23.7, 22.9, 22.7, 13.8(d, $J = 7.2$ Hz), 10.7, 0.7.

HR-MS Ultraflex III, MALDI, 370 °C; ion [M]⁺, C₂₅₂ H₂₇₄ N₈ O₈ ⁶⁴Zn₂, m/z calculated 3667.98571, m/z experimental 3668.010 ($\Delta=7$ ppm).

P- and *M*-H6Pr3

Compound *P*-H6Pr1 (7 mg, 0.002 mmol) was treated with a few drops of TFA in CH₂Cl₂ solution until the complete conversion and the formation of the free porphyrin (the progress of the reaction was carefully monitored by TLC). Then, the reaction was quenched with NaHCO₃, washed with water and then extracted with CH₂Cl₂. The organic phase was dried over MgSO₄ and the solvent was removed with pressure. The crude was immediately passed through a short plug of silica gel (CH₂Cl₂) to afford the desired product *M*-H6Pr1 in quantitative yield (6.7 mg) as a brownish solid. *M*-H6Pr3 (6.7 mg, 100 %) was obtained from *M*-H6Pr3 (7 mg, 0.002 mmol) under identical conditions.

¹H NMR (400 MHz, Chloroform-*d*) δ 10.02 (s, 2H), 9.72 (d, $J = 4.7$ Hz, 4H), 9.17 (d, $J = 4.6$ Hz, 4H), 8.93 (d, $J = 4.7$ Hz, 4H), 8.88 (d, $J = 4.5$ Hz, 4H), 8.14 – 8.05 (m, 8H), 8.00 (d, $J = 7.9$ Hz, 4H), 7.95 (d, $J = 5.4$ Hz, 4H), 7.74 (t, $J = 8.4$ Hz, 4H), 7.54 (dd, $J = 12.9, 8.0$ Hz, 6H), 7.04 (d, $J = 8.5$ Hz, 8H), 3.87 (t, $J = 6.5$ Hz, 16H), 1.12 (h, $J = 8.2$ Hz, 10H), 0.99 (q, $J = 7.0$ Hz, 28H), 0.94 – 0.81 (m, 23H), 0.73 (q, $J = 7.3$ Hz, 17H), 0.65 – 0.43 (m, 66H).

HR-MS Ultraflex III, MALDI, 370 °C; ion [M]⁺, C₂₀₆ H₂₅₂ N₈ O₈, m/z calculated 2969.98657, m/z experimental 2969.999 ($\Delta=4$ ppm).

C. NMR spectra

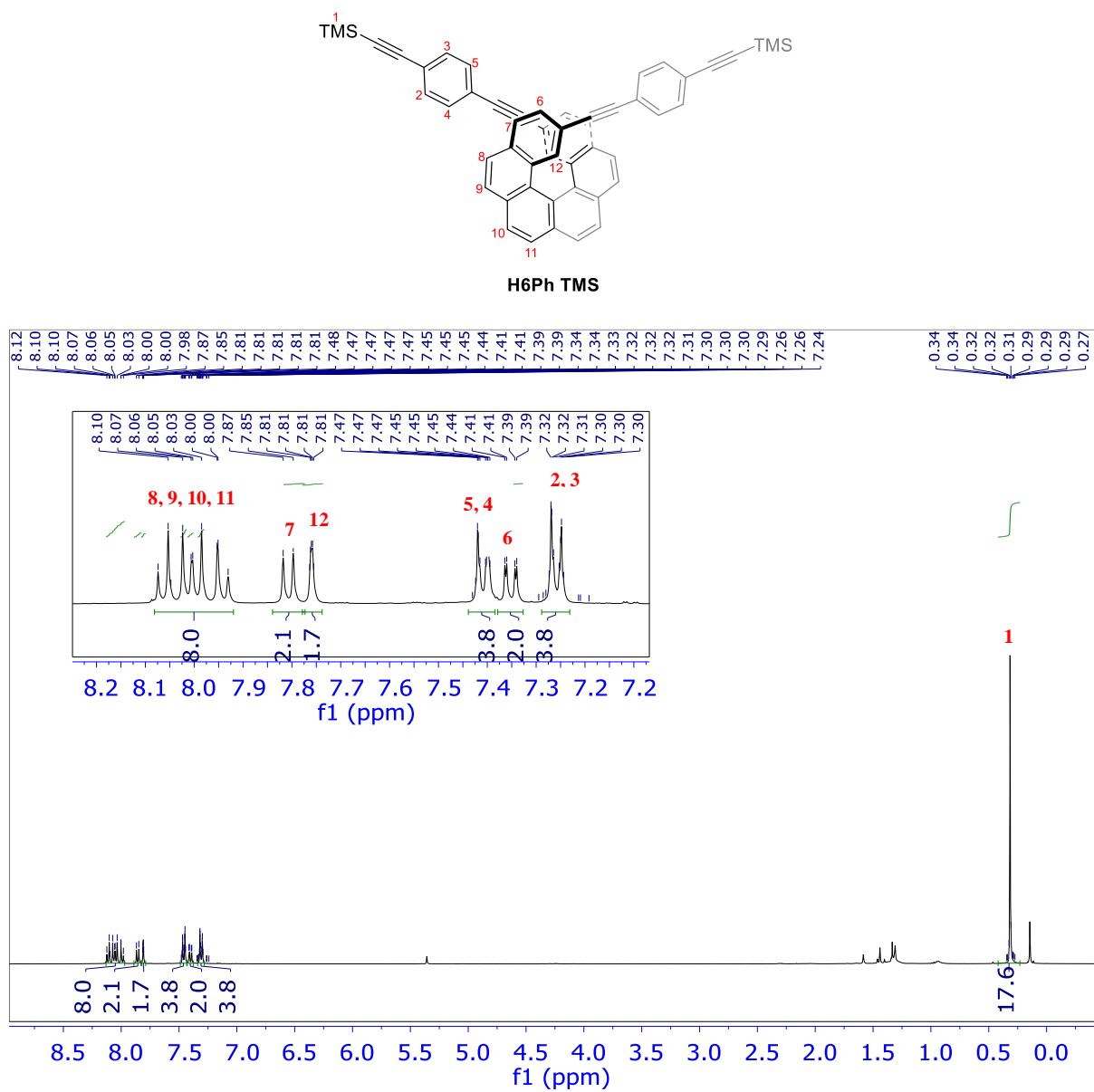


Figure S1.2. ^1H NMR spectrum of **H6PhTMS** in CD_2Cl_2 at 298 K (400MHz).

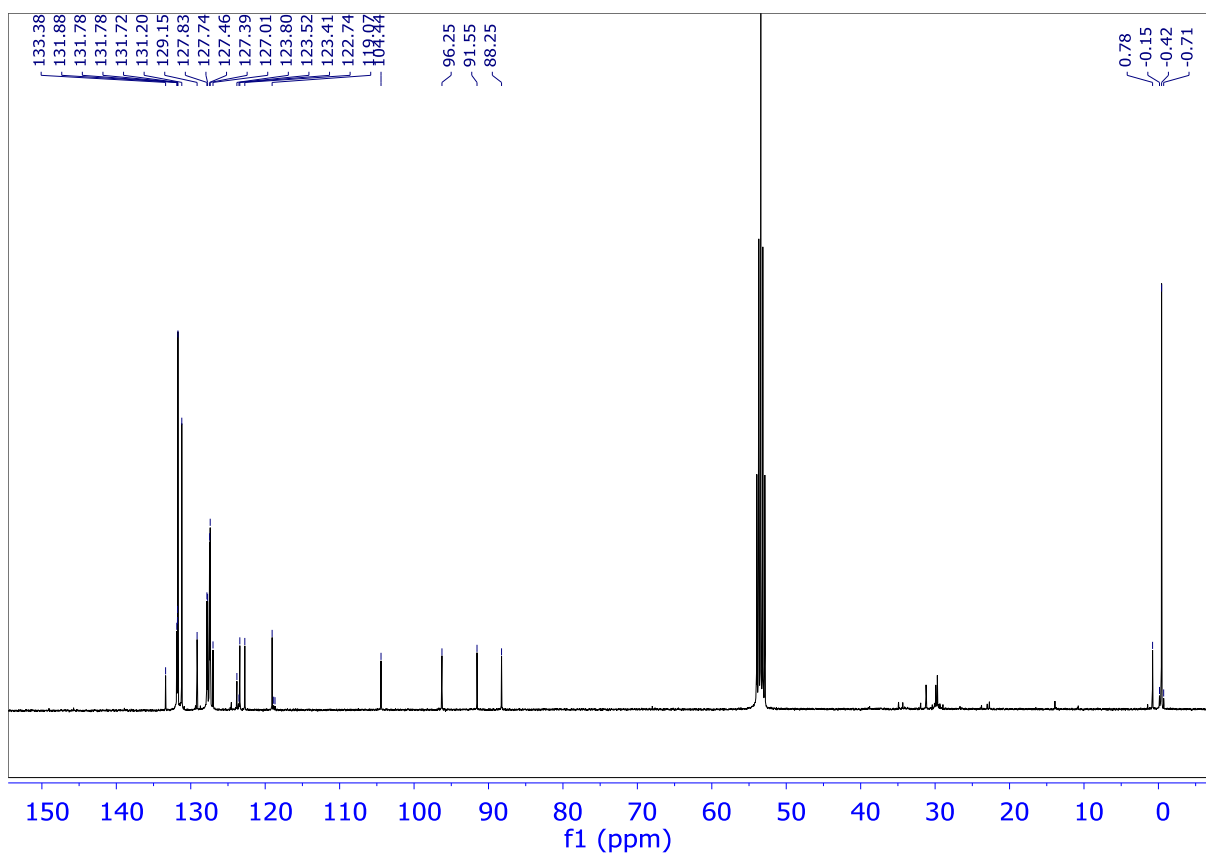
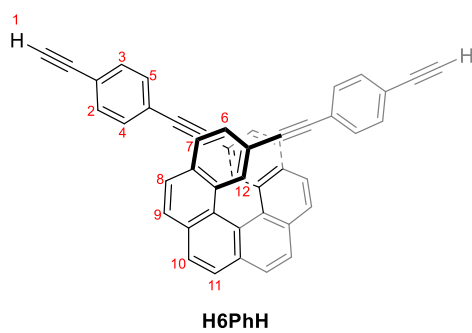


Figure S1.3. ^{13}C NMR spectrum of **H6PhTMS** in CD_2Cl_2 at 298 K (101MHz).



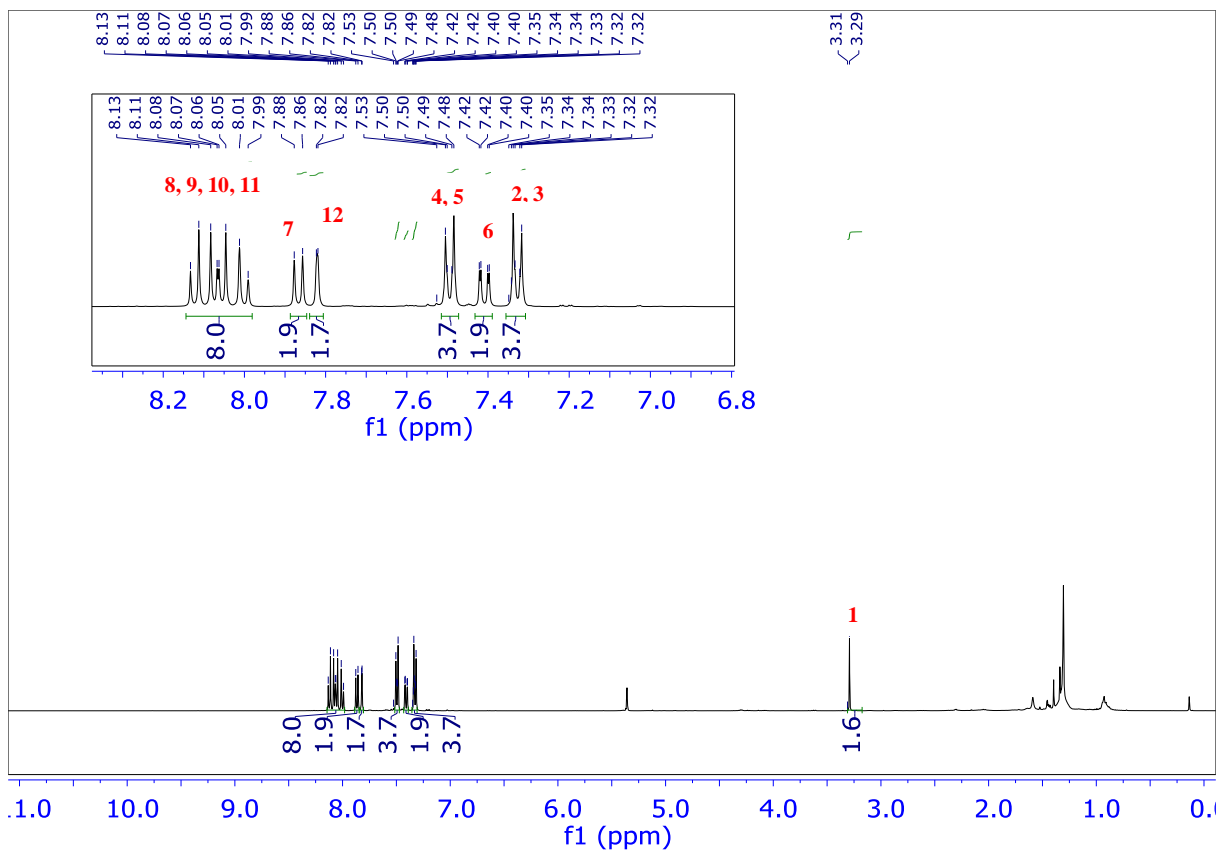


Figure S1.4. ^1H NMR spectrum of **H6PhH** in CD_2Cl_2 at 298 K (400MHz).

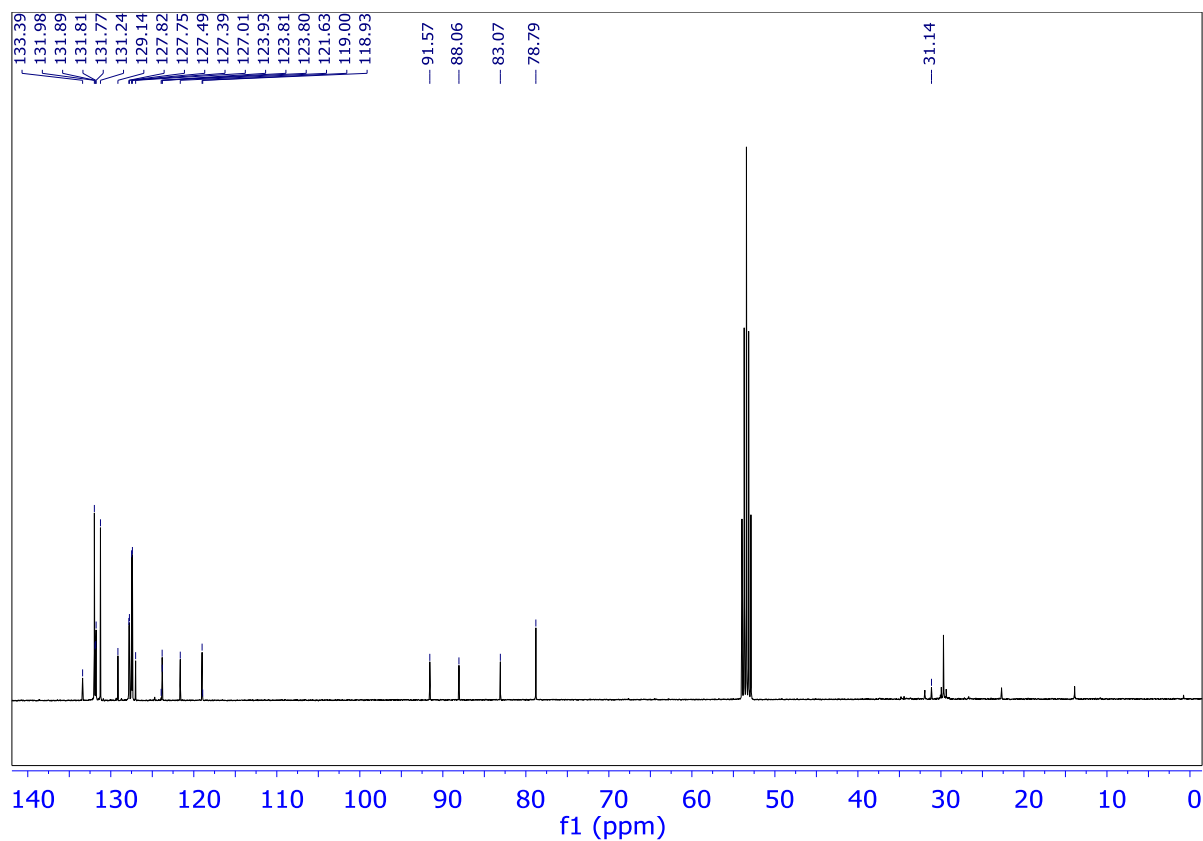


Figure S1.5. ^{13}C NMR spectrum of **H6PhH** in CD_2Cl_2 at 298 K (101MHz).

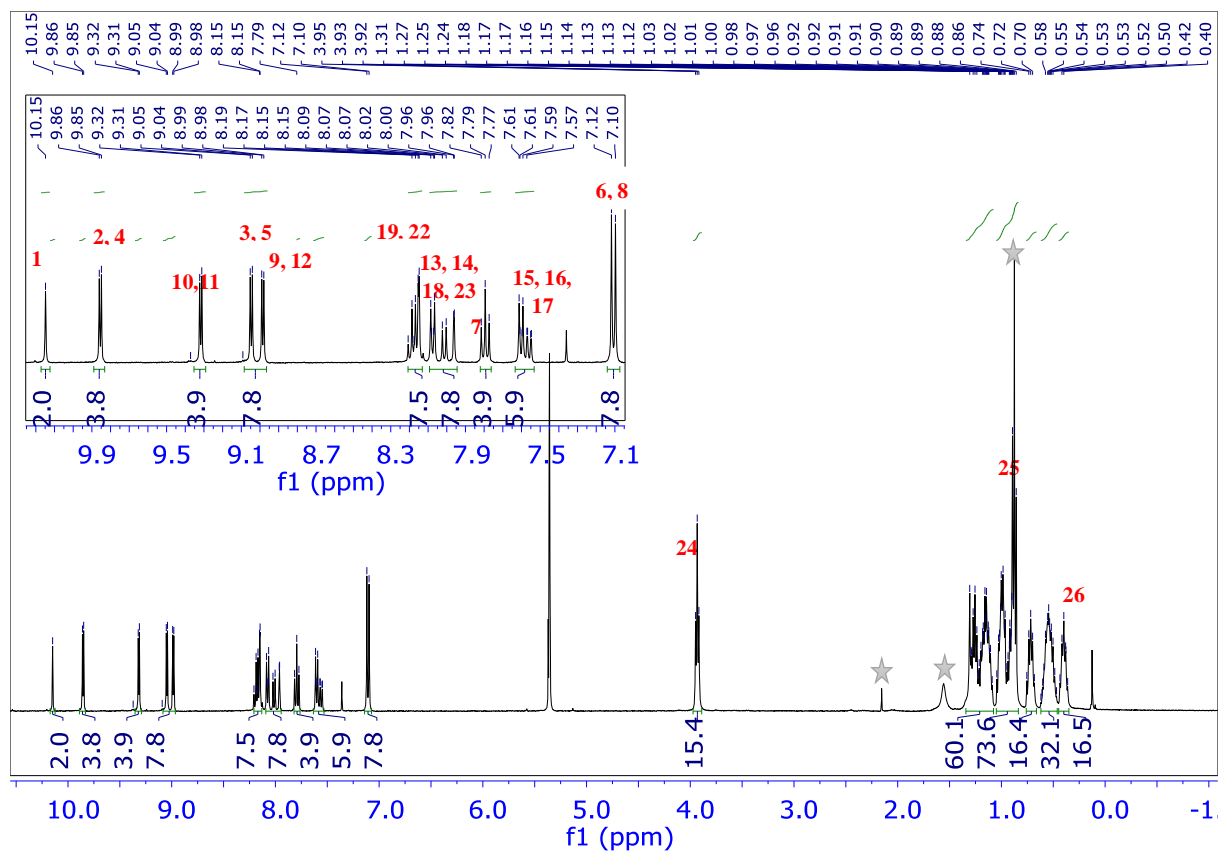
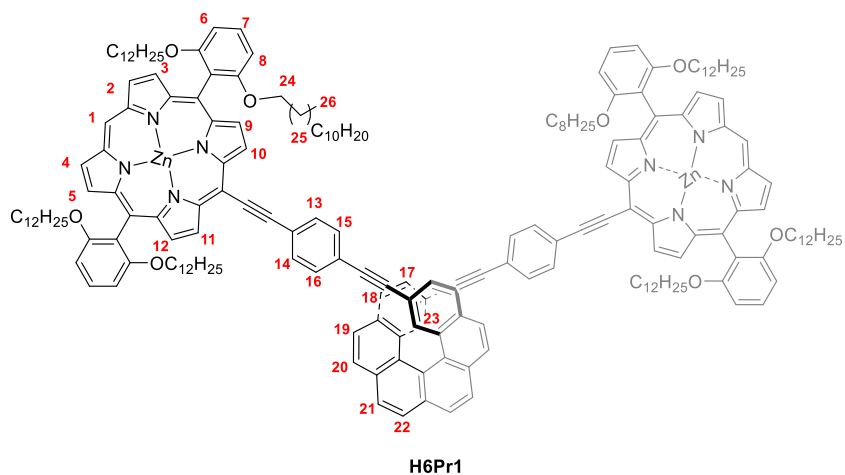


Figure S1.6. ^1H NMR spectrum of H6Pr1 in CD_2Cl_2 at 298 K (400MHz).

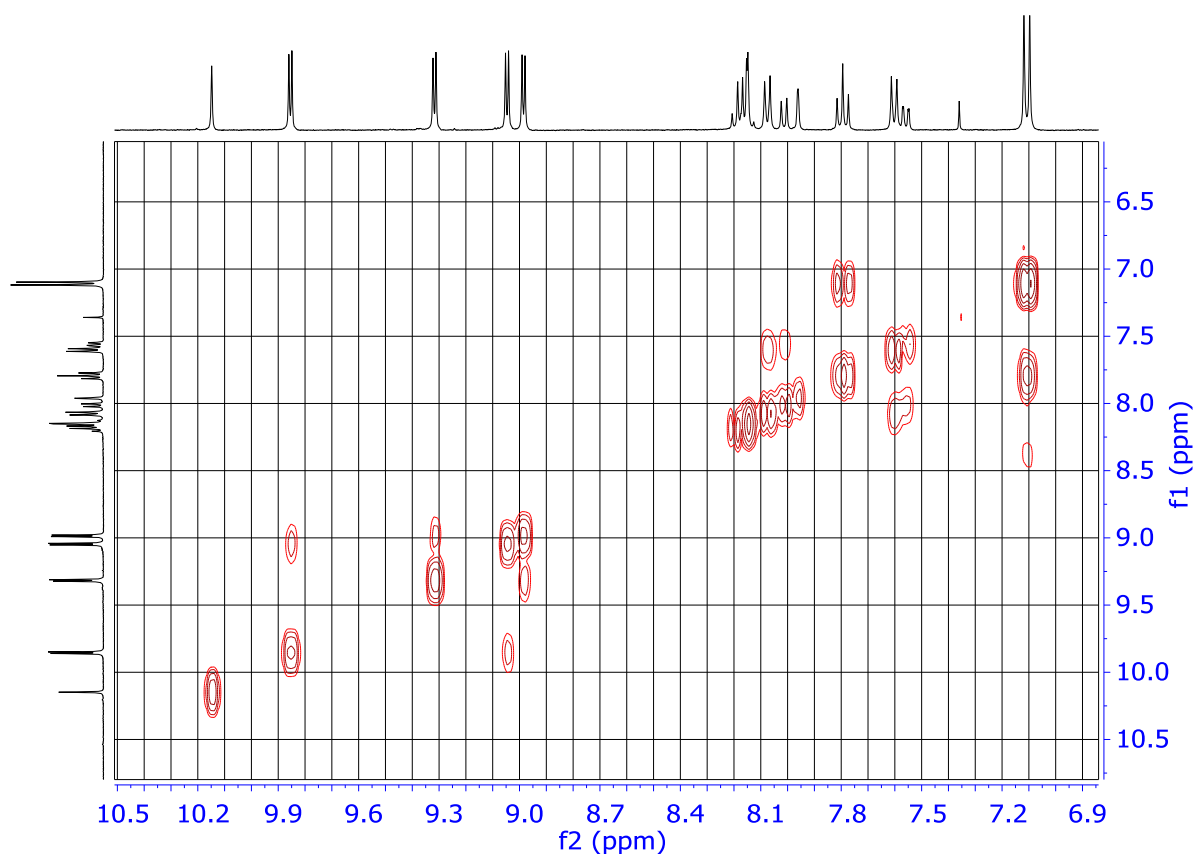


Figure S1.7. Region of the COSY spectrum of **H6Pr1** corresponding to the aromatic protons (400 MHz, CDCl₃, 298 K).

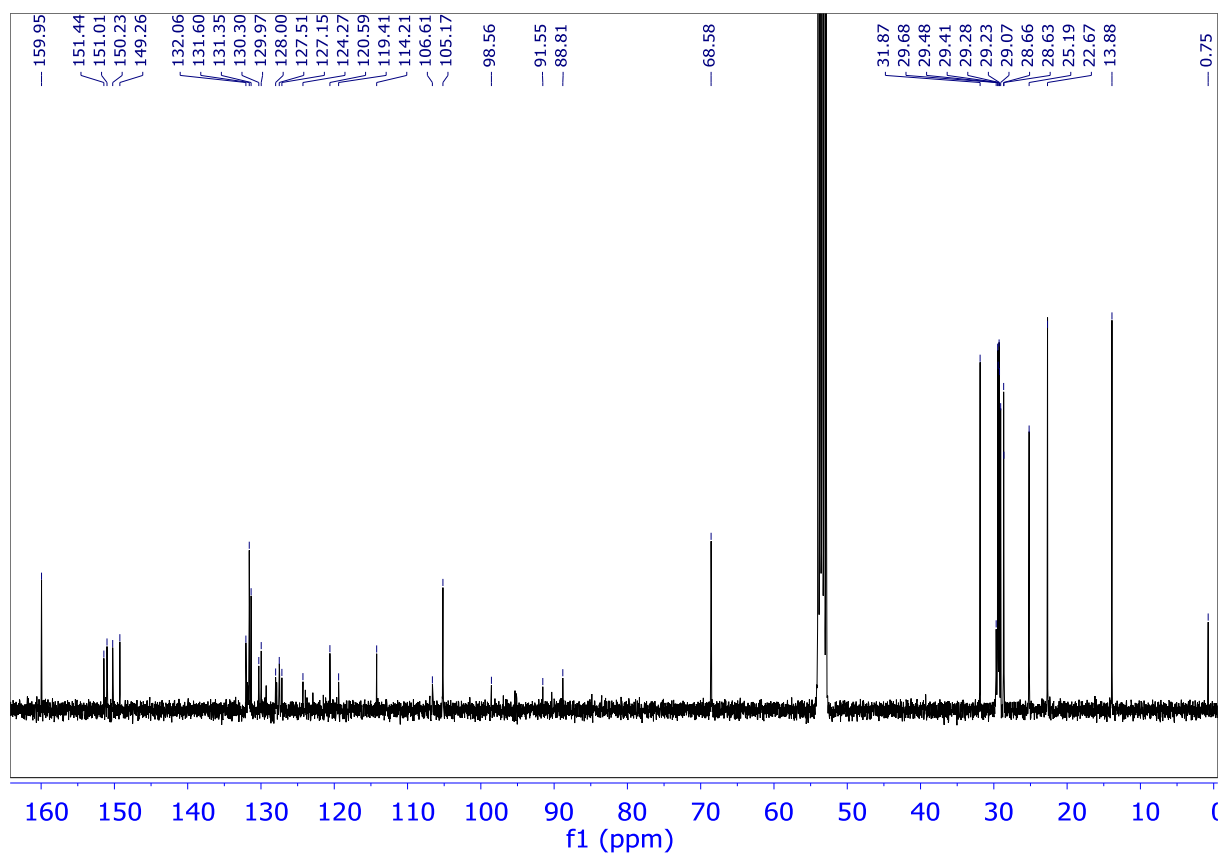
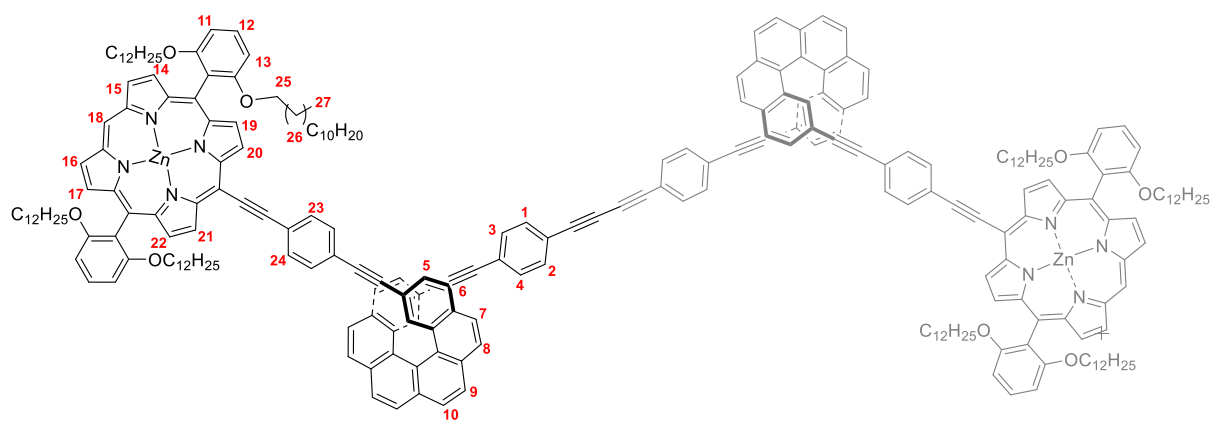


Figure S1.8. ¹³CNMR spectrum of **H6Pr1** in CD₂Cl₂ at 298 K (101MHz).



H6Pr2

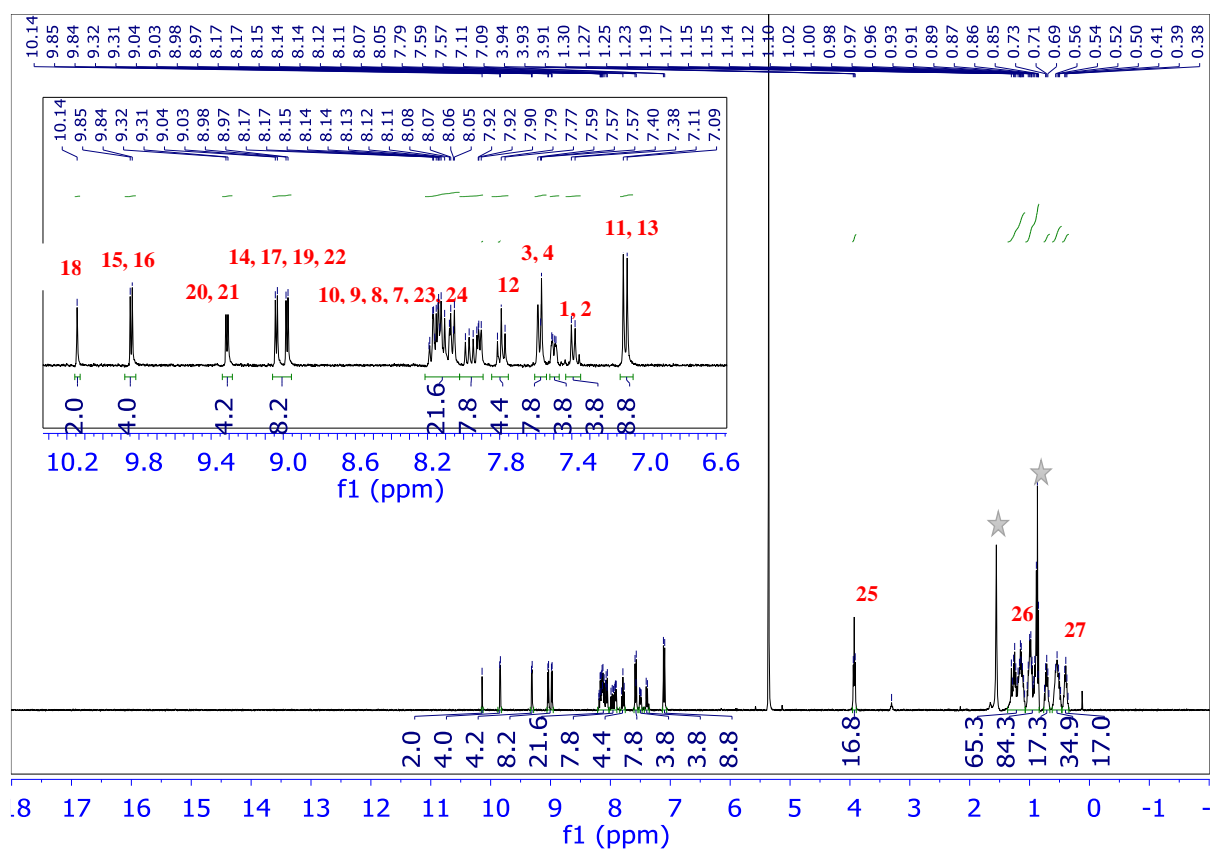


Figure S1.9. ^1H NMR spectrum of H6Pr2 in CD_2Cl_2 at 298 K (400MHz).

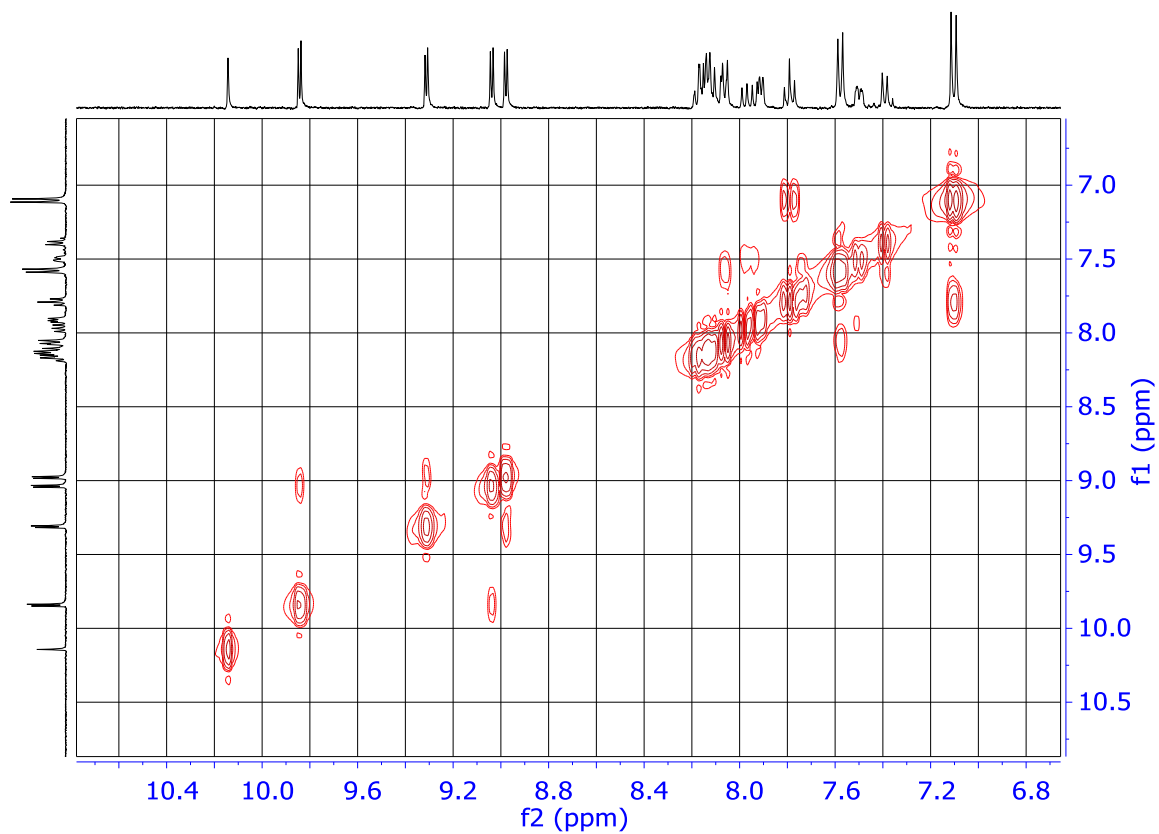


Figure S1.10. Region of the COSY spectrum of **H6Pr2** corresponding to the aromatic protons (400 MHz, CDCl₃, 298 K).

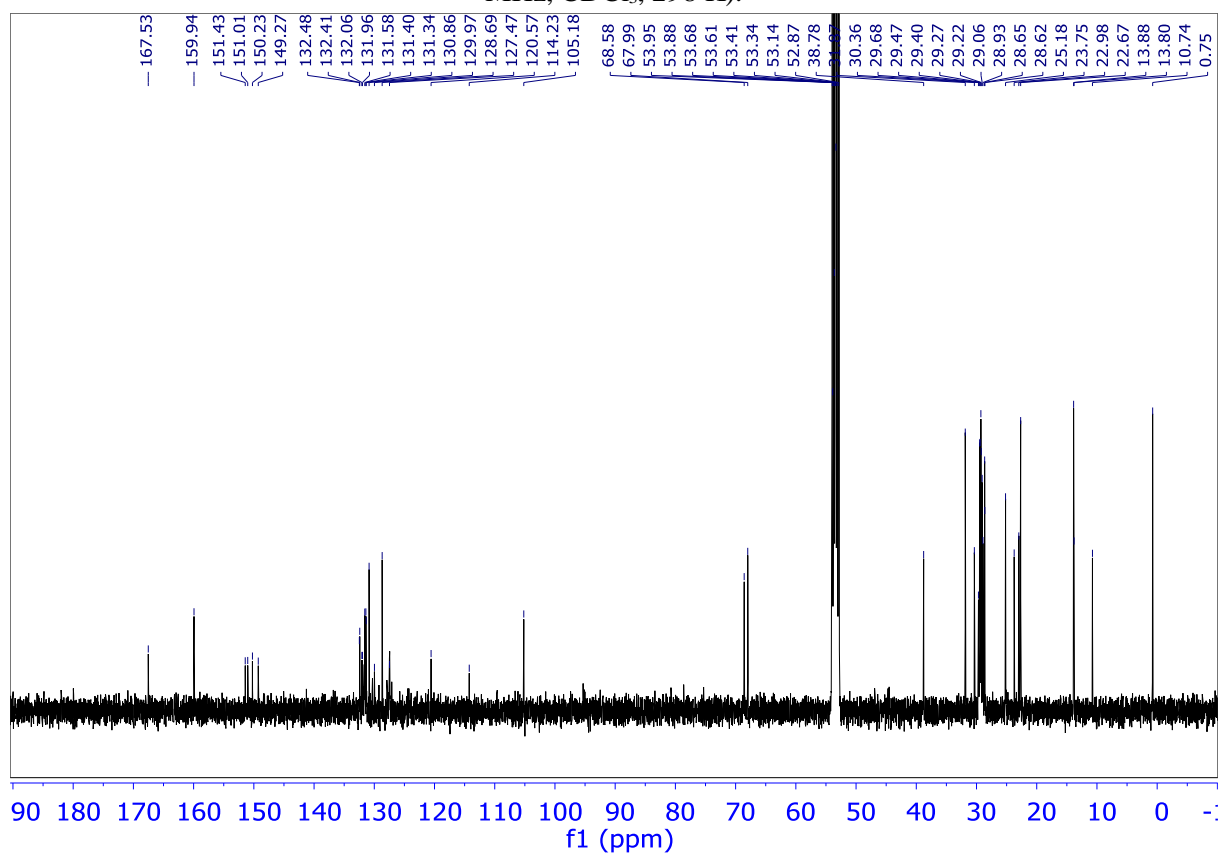


Figure S1.11. ¹³CNMR spectrum of **H6Pr2** in CD₂Cl₂ at 298 K (101MHz).

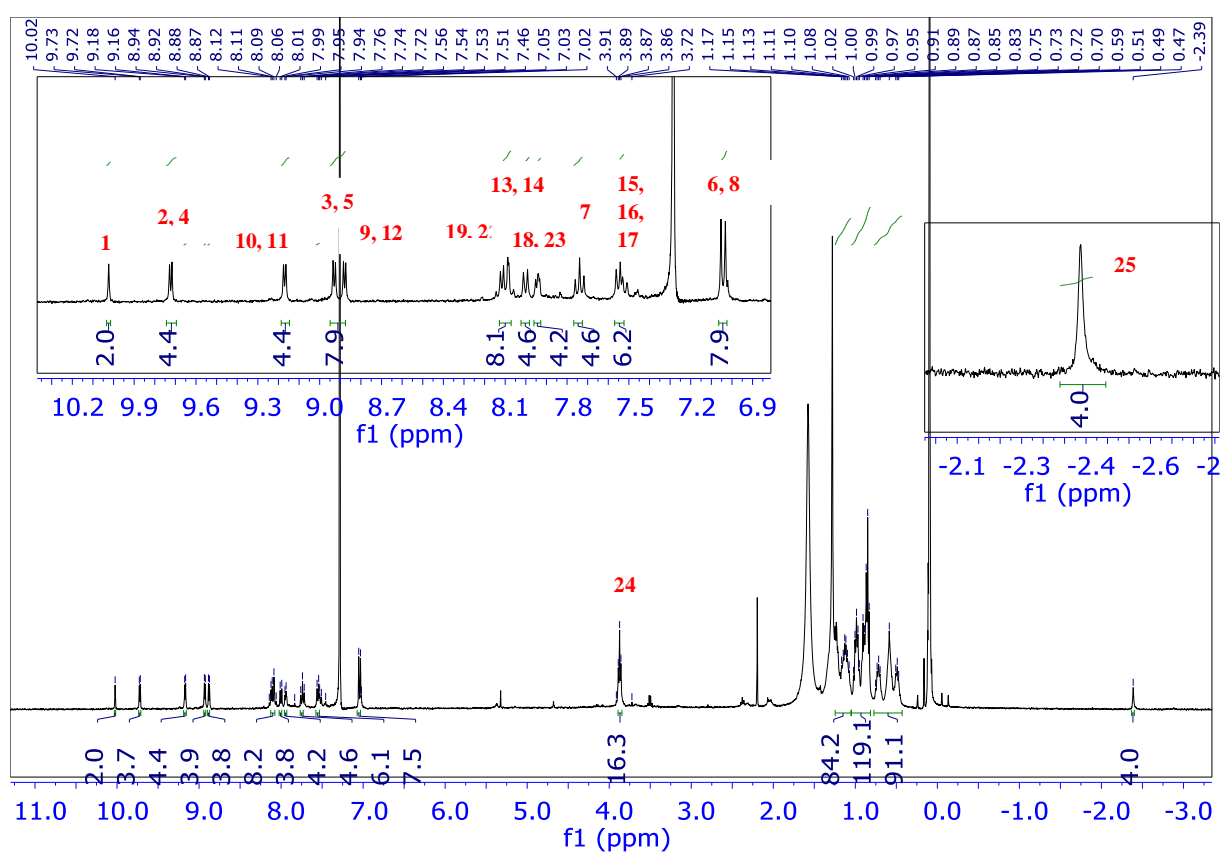
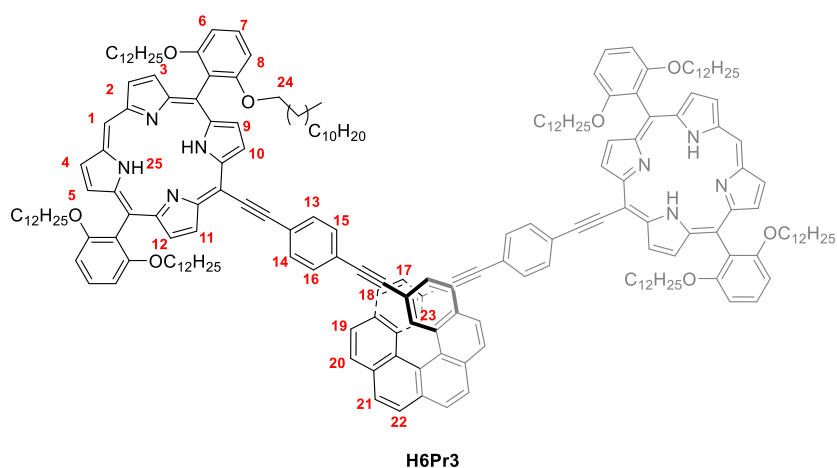


Figure S1.12. ¹H NMR spectrum of H6Pr3 in CDCl₃ at 298 K (400MHz).

D. MALDI-TOF spectra

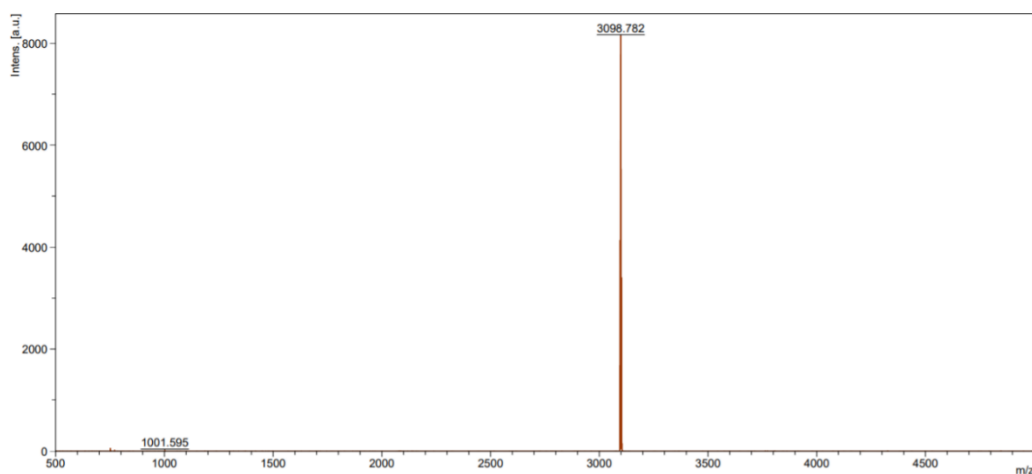


Figure S1.13. MALDI mass spectrum of the **H6Pr1** in the positive ion mode. The matrix was **DCTB** (trans-2-[3-(4-tert-Butylphenyl)-2-methyl-2-propenylidene]malononitrile).

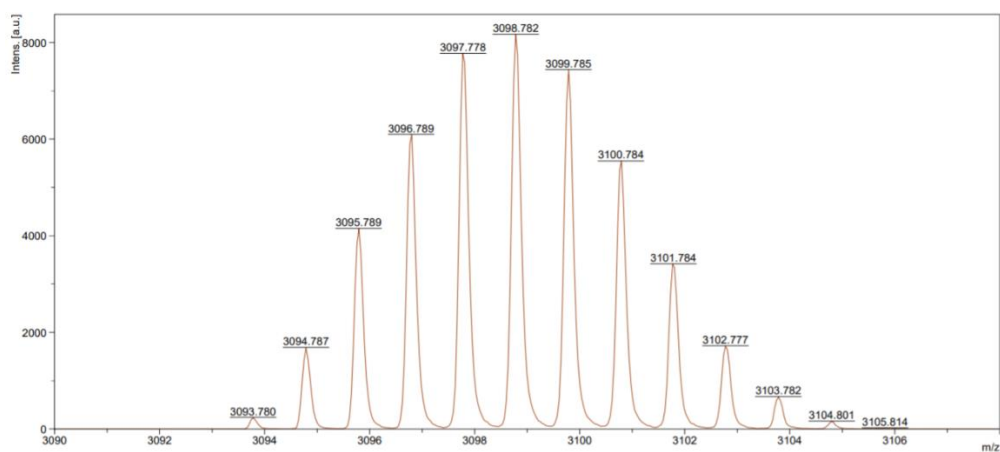


Figure S1.14. MALDI-MS enlarged spectrum of the **H6Pr1**.

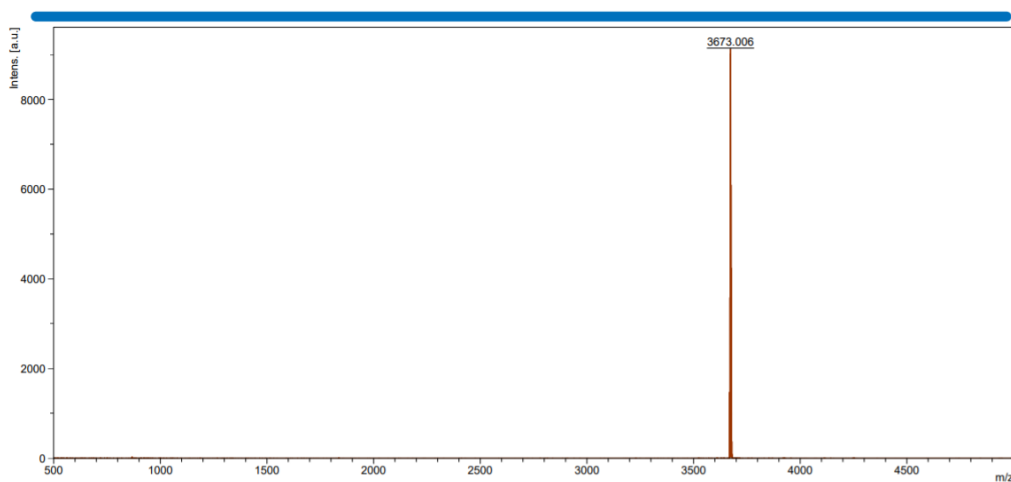


Figure S1.15. MALDI mass spectrum of the **H6Pr2** in the positive ion mode. The matrix was **DCTB**.

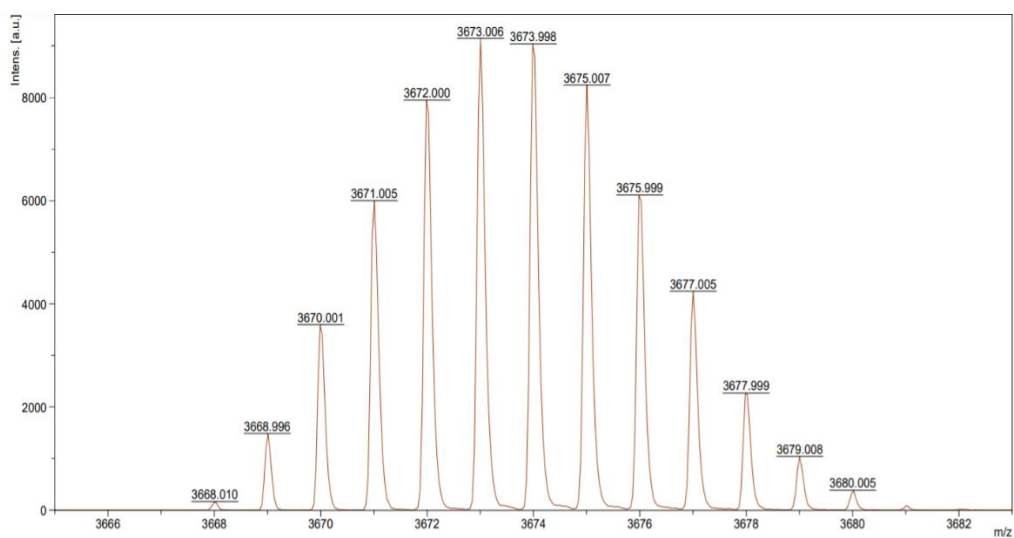


Figure S1.16. MALDI-MS enlarged spectrum of the **H6Pr2**.

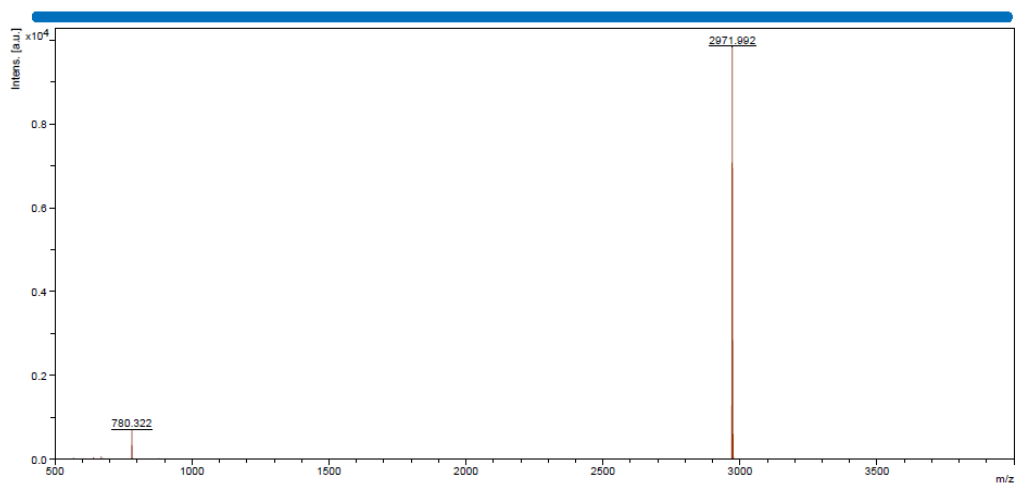


Figure S1.17. MALDI mass spectrum of the **H6Pr3** in the positive ion mode. The matrix was **DCTB**.

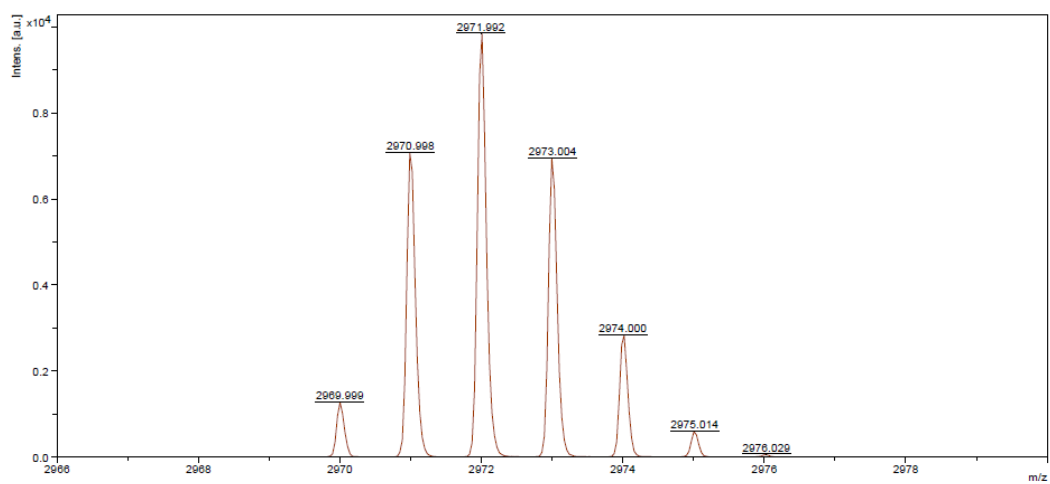


Figure S1.18. MALDI-MS enlarged spectrum of the **H6Pr3**.

E. Photophysical characterization

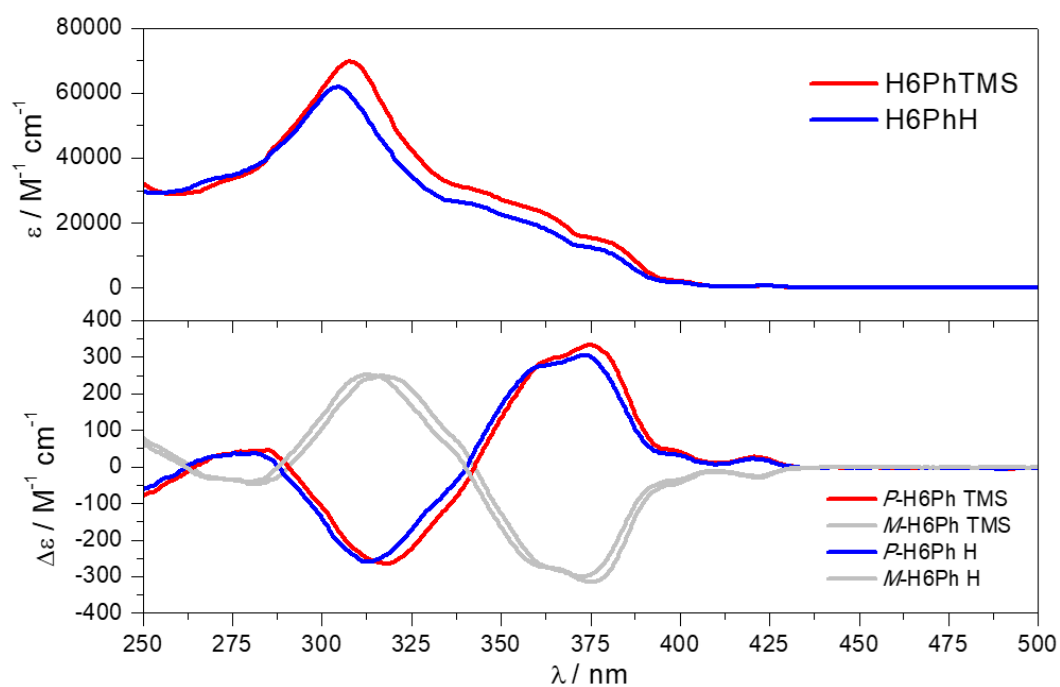


Figure S1.19. Epsilon (top) and ECD (bottom) spectra of **H6PhTMS** (red) and **H6PhH** (Blue) in dichloromethane solution ($\sim 10^{-6}$ M) at 298 K (*M* enantiomers are shown in grey).

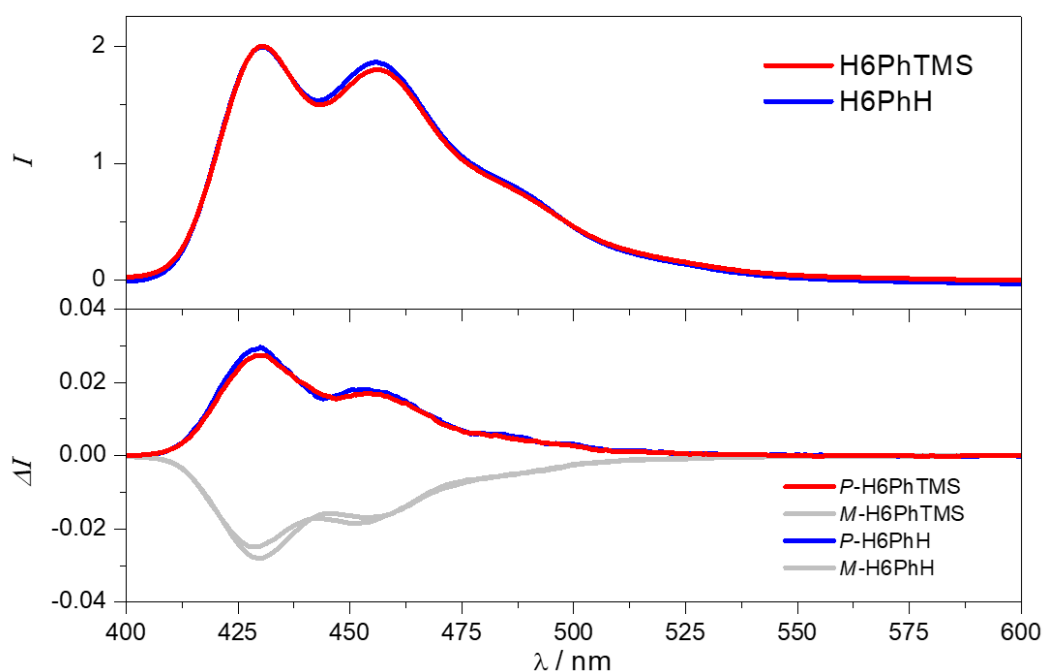


Figure S1.20. Normalized fluorescence (top) and CPL (bottom) spectra of **H6PhTMS** (red) and **H6PhH** (Blue) in dichloromethane solution ($\sim 10^{-6}$ M) at 298 K (*M* enantiomers are shown in grey).

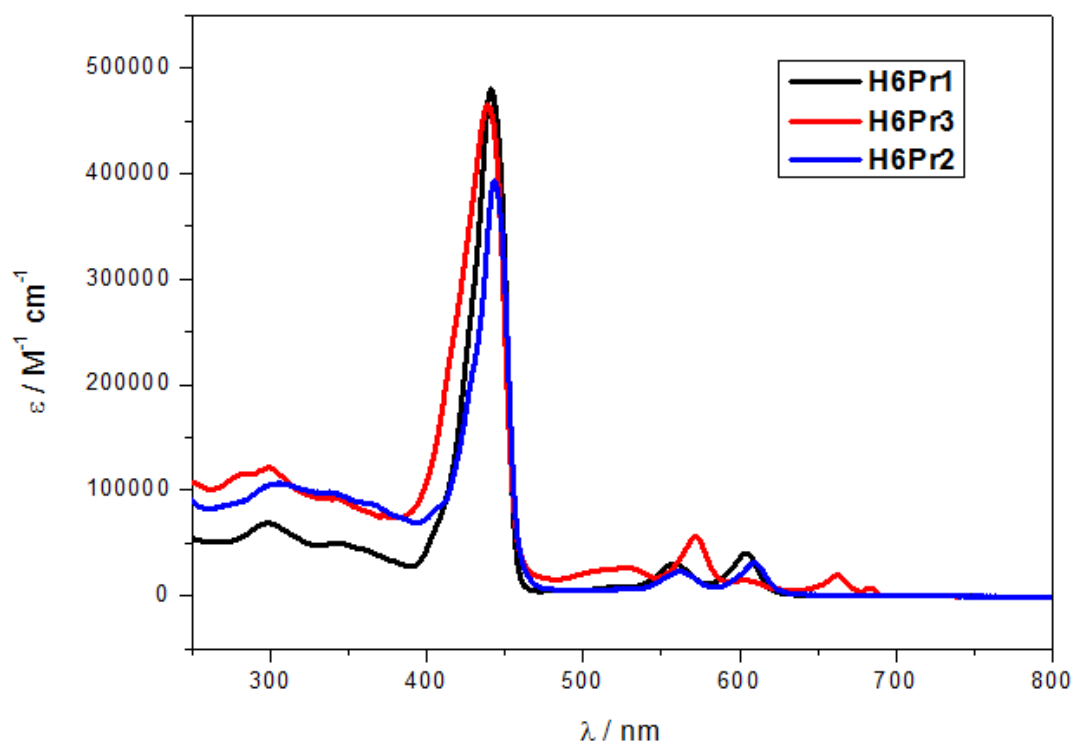


Figure S1.21. Epsilon spectra of **H6Pr1** (black), **H6Pr2** (blue) and **H6Pr3** (red) in dichloromethane solution ($\sim 10^{-6}$ M) at 298 K.

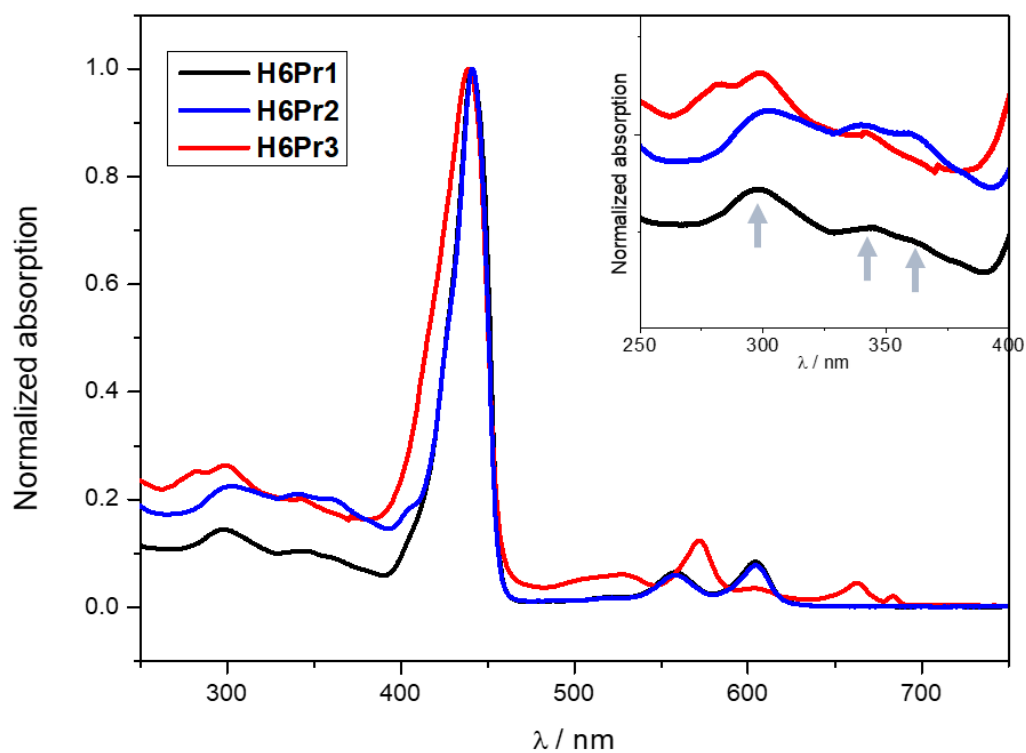


Figure S1.22. Normalized absorption spectra of **H6Pr1** (black), **H6Pr2** (blue) and **H6Pr3** (red) in dichloromethane solution ($\sim 10^{-6}$ M) at 298 K.

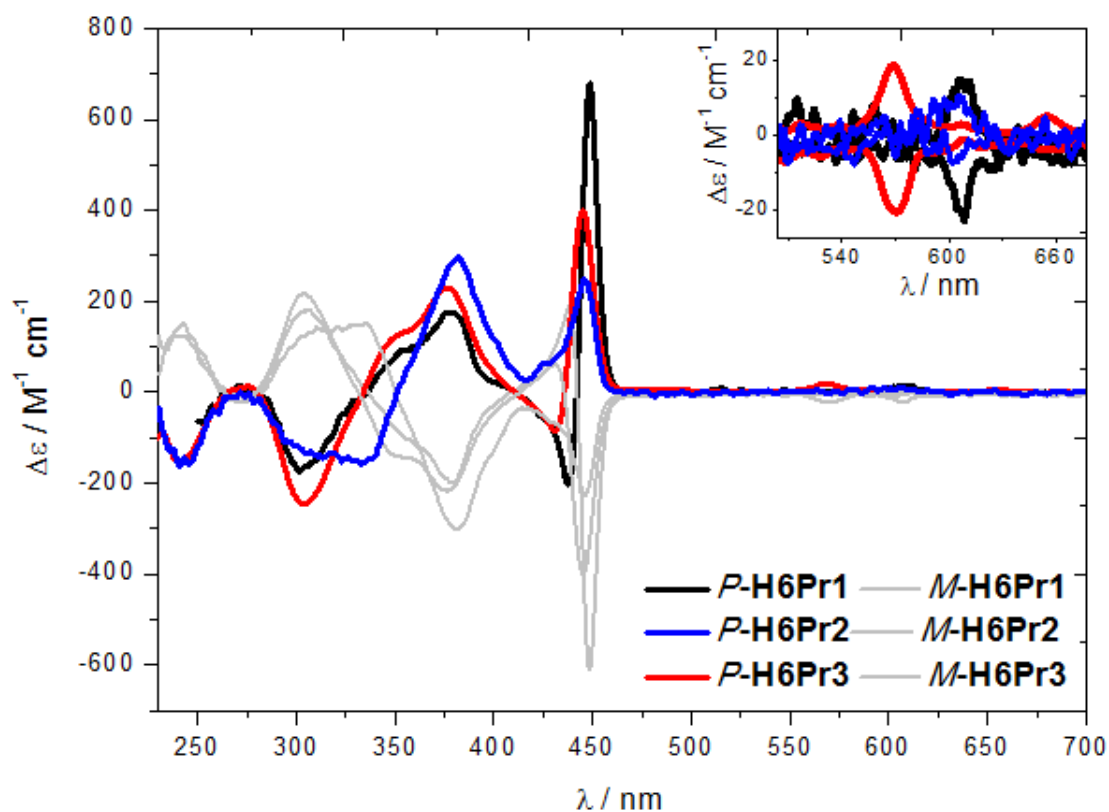


Figure S1.23. ECD spectra of **H6Pr1** (black), **H6Pr2** (blue) and **H6Pr3** (red) in dichloromethane solution ($\sim 10^{-6}$ M) at 298 K (*M* enantiomers are shown in grey).

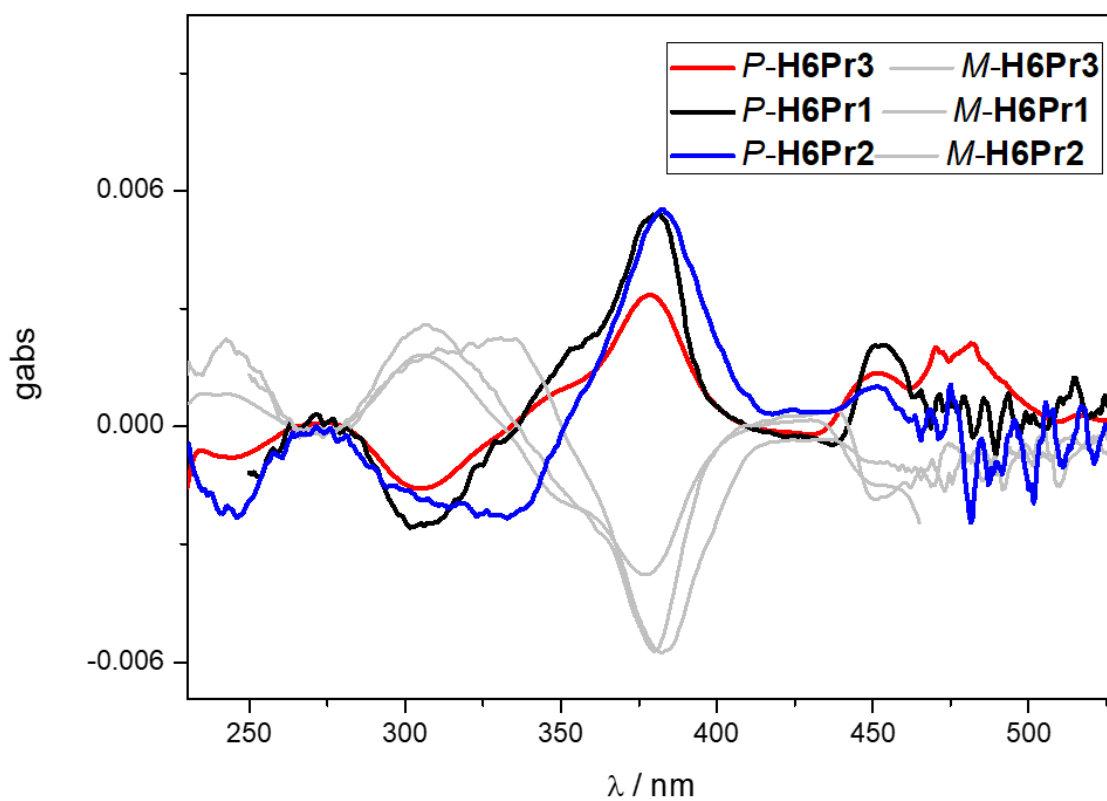


Figure S1.24. g_{abs} spectra of **H6Pr1** (black), **H6Pr2** (blue) and **H6Pr3** (red) in dichloromethane solution ($\sim 10^{-6}$ M) at 298 K (*M* enantiomers are shown in grey).

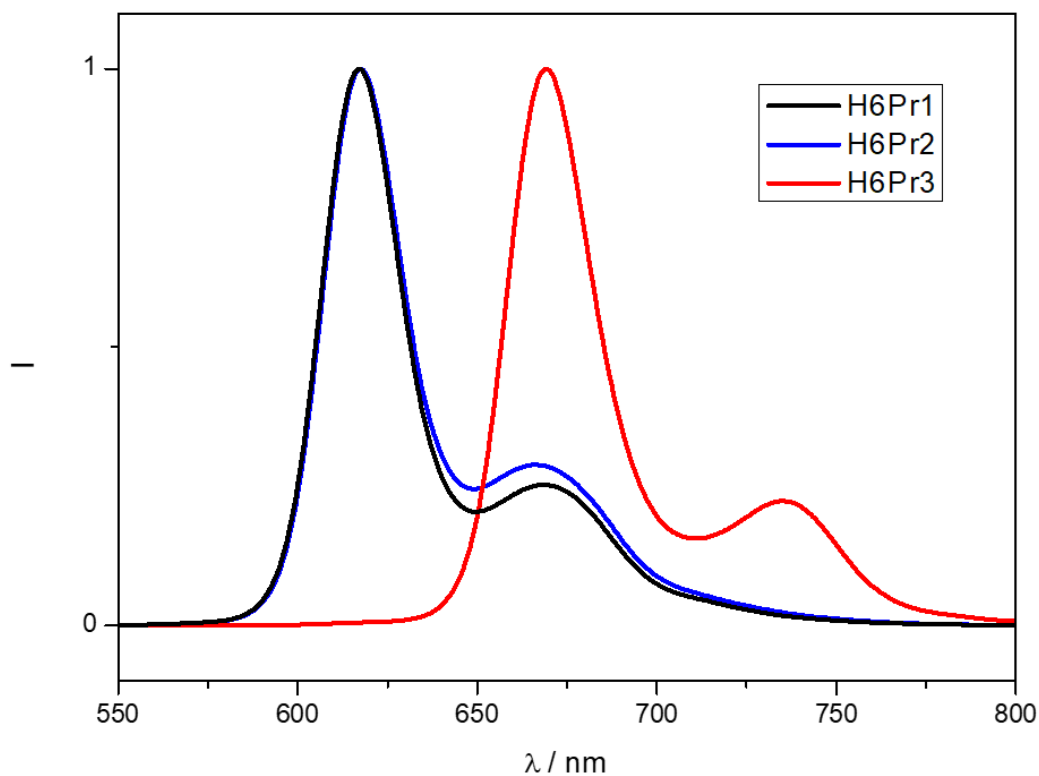


Figure S1.25. Normalized emission spectra of **H6Pr1** (black), **H6Pr2** (blue) and **H6Pr3** (red) in dichloromethane solution ($\sim 10^{-6}$ M).

Table S1.1. Quantum yields (averaged values) of fluorescence for **H6Pr1**, **H6Pr2** and **H6Pr3** and g_{lum} values

Compound	ϕ	g_{lum}	λ_{em}
H6Pr1	0.16 ^a	$\pm 7 \cdot 10^{-4}$	617 nm
H6Pr2	0.25 ^a	$\pm 7 \cdot 10^{-4}$	617 nm
H6Pr3	0.22 ^a	$\pm 2 \cdot 10^{-4}$	670 nm

^a Fluorescence quantum yields measured in distilled toluene using Tetraphenylporphyrin (TPP) (Figure S1.26) ($\phi_f = 11\%$) as standard upon excitation at the Soret band.⁵

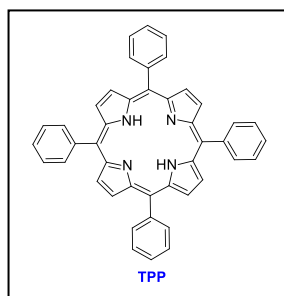


Figure S1.26. Chemical structure of Tetraphenylporphyrin (TPP)

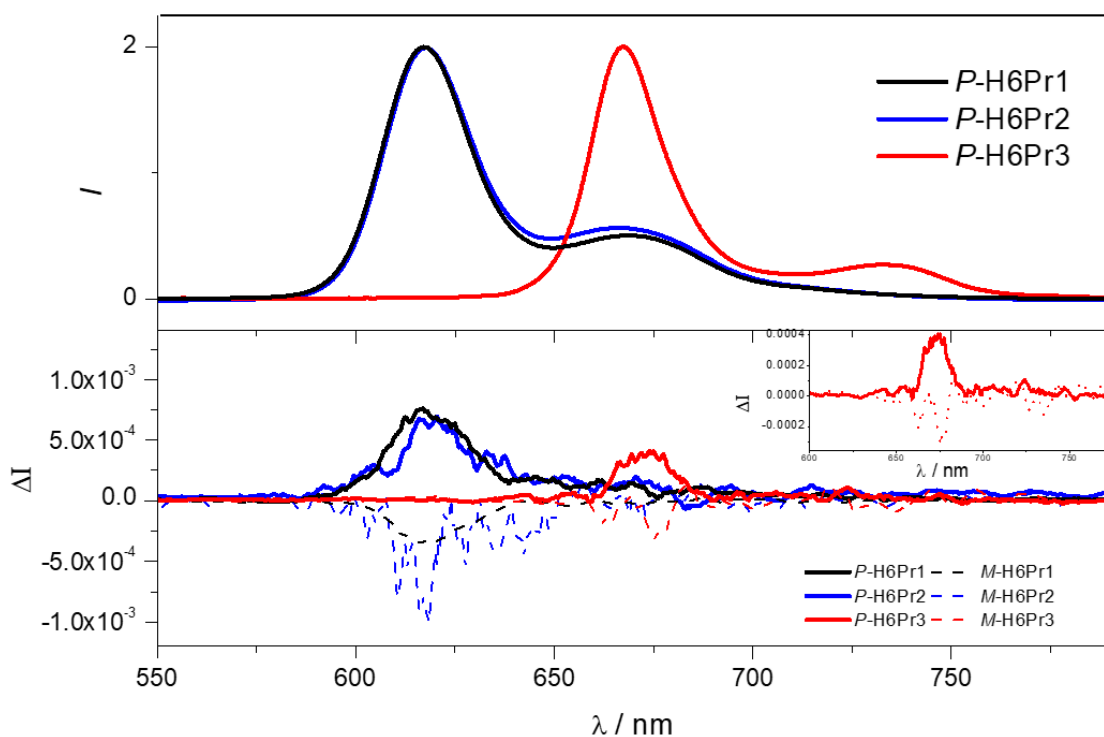


Figure S1.27. Comparison of normalized fluorescence (top) and CPL (bottom) spectra of *P* (plain lines) and *M* (dashed lines) enantiomers of **H6Pr1** (black), **H6Pr2** (blue) and **H6Pr3** (red) in dichloromethane solutions ($\sim 10^{-6}$ M) at 298 K.

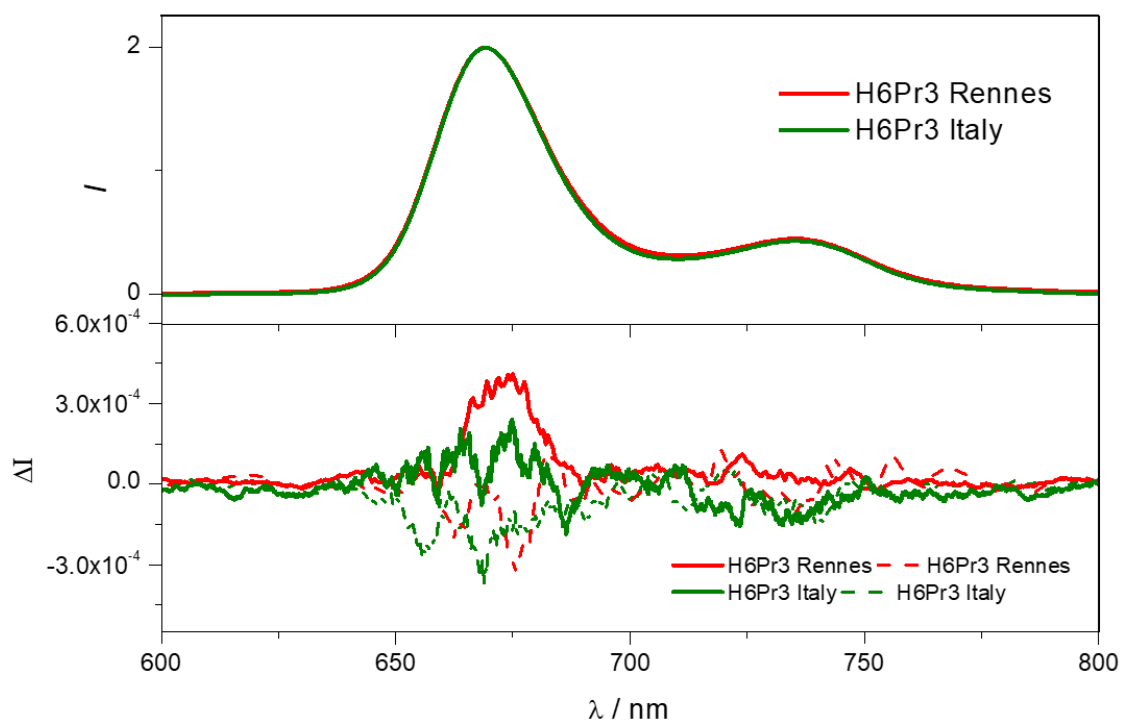


Figure S1.28. Comparison of normalized fluorescence (top) and CPL (bottom) spectra of *P* (plain lines) and *M* (dashed lines) enantiomers of **H6Pr3** measured on a home-built CPL apparatus in Rennes (red) and on a commercial one (green) in Italy (CH_2Cl_2 , $\sim 10^{-6}$ M) at 298 K.

III. Computational part

Computational Details

All computations were performed with the Gaussian 16⁶ (G16) package using Kohn-Sham density functional theory (DFT). The B3LYP functional⁷ and the def2-SV(P) basis set^{8,9} were selected for geometry optimizations and vibrational normal mode calculations. The polarizable continuum model (PCM)¹⁰ for dichloromethane was used to simulate solvent effects.

Absorption and electronic circular dichroism (ECD) spectra were calculated from time-dependent DFT (TD-DFT) linear response calculations of the lowest 200 vertical singlet electronic excitations. We utilized the def2-SV(P) basis and a functional based on PBE0¹¹ with range-separated exchange and correct asymptotic behavior (long-range correction (LC))^{12,13}. The LC-PBE0 parametrization afforded 25% of exact exchange in the short-range limit and used an error-function range-separation with $0.30 a_0^{-1}$ as the separation parameter (γ). Test calculations were performed with γ values used in previous theoretical studies of tetraphenylporphyrin exciton coupling and optical rotation of helicene derivatives.^{14,15} Empirical Gaussian broadening of the calculated intensities, corresponding to a of σ 5 wavenumbers times the square root of the transition wavenumber value, was applied to generate spectral envelopes for comparison with the experiments. Solvent effects for dichloromethane were also considered in the TD-DFT calculations. For overviews of the general performance of TD-DFT for chiroptical spectra, see, for example, References^{16,17}.

Computational Results

Due to the large number of atoms in **H6Pr1** in substituents that do not contribute to the long-wavelength spectral properties, all computational analyses were performed on a truncated system where the Ph(OR)_2 substituents at the Zn-porphyrin units were replaced by chlorine atoms, denoted here as **H6Pr1-Cl**. The optimized structure of *P*-**H6Pr1-Cl** is displayed in Figure S2.1. We note that the first transition of the benzene-(OCH₃)₂ system is at 243 nm, indicating that the use of Cl instead of Ph(OR)_2 should be insignificant in the spectra at longer wavelengths. Test calculations of spectra for **H6Pr1-CH₃**, i.e. a model replacing Ph(OR)_2 by methyl, showed qualitatively similar results as **H6Pr1-Cl**, but the band positions compared less well with the experiments. An additional test calculation showed near-perfect agreement between the ECD spectrum of **H6Pr1-Cl** and that of a larger model for **H6Pr1** including the phenyl rings (replacing O-alkyl groups by chlorine atoms) below 250 nm, owing to the fact that the phenyl rings are perpendicular to the Zn-porphyrin planes and are therefore not part of the π -chromophore. Moreover, the UV transitions of phenyl are weakly intense and do not cause significant exciton coupling in **H6Pr1**. Hence, **H6Pr1-Cl** is a good model for **H6Pr1** for the purpose of this study. Therefore, we refer to calculations for the model by the **H6Pr1** label in the following, unless the distinction needs to be specifically noted.

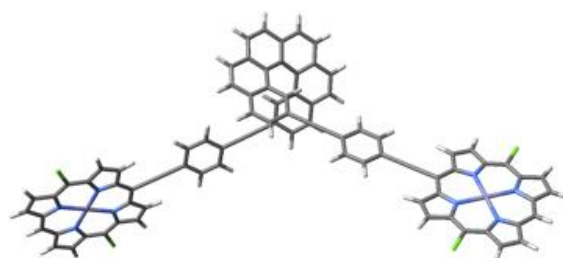


Figure S2.1. DFT-optimized structure of model *P-H6Pr1-Cl*.

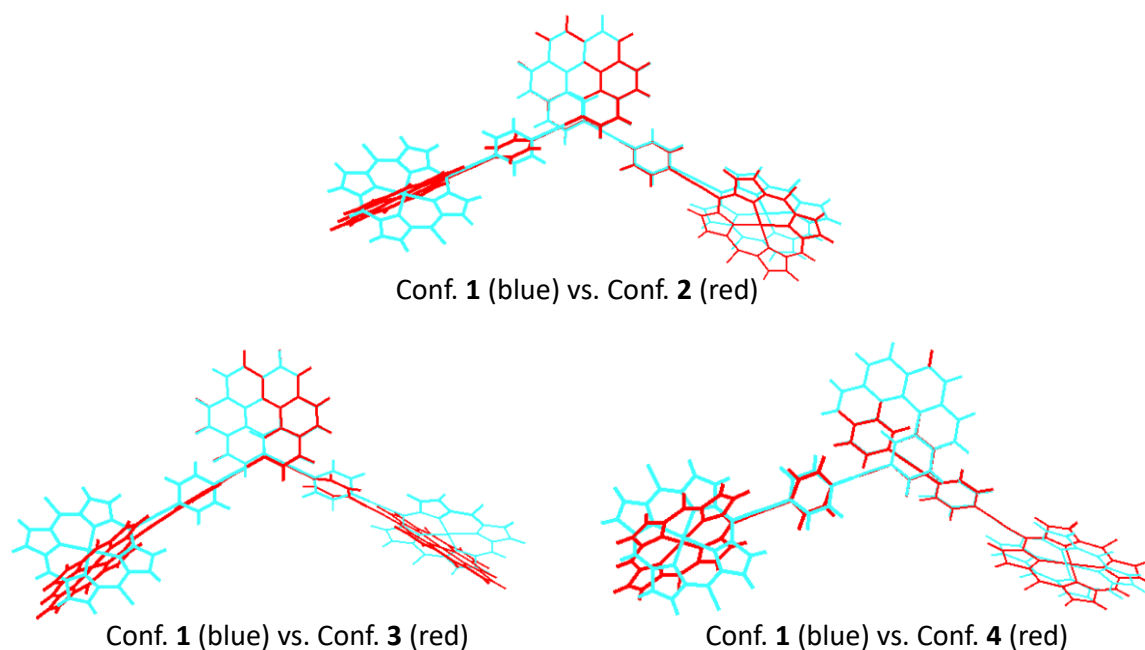


Figure S2.2. Comparison of different DFT-optimized conformers (Conf.) of model *P-H6Pr1-Cl*. Conformer 1 (in blue) is the one shown in Figure S2.1.

Table S2.1. Relative energies (in kcal·mol⁻¹) and Boltzmann population at 298.15 K (in %) for the different conformers considered of *P-H6Pr1-Cl*. Conformer 1 is the one shown in Figure S2.1.

Conformer	Relative Energy	Boltzmann population
1	0.0	67
2	0.9	15
3	2.1	2
4	0.8	16

Absorption Spectroscopy. The calculated UV/Vis spectrum for **H6Pr1-Cl** is shown in Figure S2.3. The simulated absorption spectrum agrees very well with the experimental one for **H6Pr1**, with the peaks systematically blue shifted by 0.3 eV in the calculations (see Scheme S2.1). This shift is due to the combination of approximations made in the TD-DFT calculations, and its magnitude is not out of the ordinary. Here, in particular, the long-range correction (LC) in the functional tends to cause a blue-shift, but it is absolutely essential, to avoid spurious charge-transfer transitions among the porphyrins, in particular.¹⁴

Different spectral regions with distinct intensities can be identified for **H6Pr1**. Isosurfaces of the corresponding molecular orbitals (MOs) associated with the most intense excitations (Table S2.2) are shown in Figure S2.4. Table S2.2 also gives a breakdown of the transition densities in terms of pairs of occupied-unoccupied (occ-unocc) MOs, to assist the assignment of the excitations. However, as it is typical in calculations with functionals that have an overall large fraction of exact exchange, there tends to be strong admixture of occ-unocc contributions in most excitations. The assignments are based on the leading occ-unocc pair contributions.

In reference to the Gouterman model¹⁸ notation for porphyrin, if the Zn-porphyrin units in the system were connected not by a chromophore, we would expect weak spectral features from the Q bands around 2 eV, strong intensity from the Soret (B) bands around 3.5 eV, and moderately intense features from the N bands, with excitonic features in each case. The weak lowest-energy / longest wavelength band in the **H6Pr1** spectrum is caused by an effectively degenerate pair of transitions, #1 and #2. The contributing MOs are composed of in-phase and out-of-phase π and π^* porphyrin fragment frontier orbitals (FFOs), with the small energetic splitting indicating that the contributing FFOs are only weakly coupled. Excitations #1 and #2 correspond to an exciton-coupled set of porphyrin Q band transitions. The frontier MOs (FMOs) in **H6Pr1-Cl** are mostly localized on the porphyrins, but several of the MOs also extended over the π -conjugated systems of the phenyl (Ph) ring and the alkynyl (CC) groups, and reach into the helicene. These MOs are therefore clearly perturbed, relative to isolated Zn-porphyrin MOs. The second set of excitations, #3 and #4, around 2.1 eV, is assigned to coupling of the remaining Q-band porphyrin transitions. The experimental spectrum shows some intensity in this region, unlike the calculation.

The Soret band in the absorption spectrum has 4 underlying transitions in the calculation, and formally arise from the coupling of the two $\pi \rightarrow \pi^*$ B-band excitations in each porphyrin. Excitation #5, at 395 nm, has by far the largest oscillator strength (4.882), and the leading contributions involve MOs that are mostly, but not entirely, porphyrin-centered. Relative to an isolated Zn-porphyrin model (see Additional Information), the excitations in **H6Pr1** appear at lower energy, due to the larger extension of the π chromophore through the linker toward the helicene. Excitations #6 and #8, under the same band, have

important contributions from the HOMO-2, which is a helicene π orbital. The excitations therefore have mixed character of helicene-to-porphyrin charge transfer (CT) and porphyrin $\pi \rightarrow \pi^*$. We note that the energetic spacing between the Q- and B-band excitations is improved with a smaller range separation parameter γ in the LC functional (see, in the Additional Information, Figures S2.20 and S2.21). However, since our focus is on the B-band exciton CD and γ of $0.30 a_0^{-1}$ reproduces the positive band following the B-band couplet (after a global red shift), we decided to proceed with those spectra.

The bands below 350 nm are of strongly mixed character, with varying porphyrin – linker – helicene contributions. The most common assignment, based on the leading occ-unocc MO pair contributions is porphyrin to helicene-CC-Ph-CC and π -helical core to helicene-CC-Ph-CC charge transfers (CT), without cleanly identifiable porphyrin N band transitions.

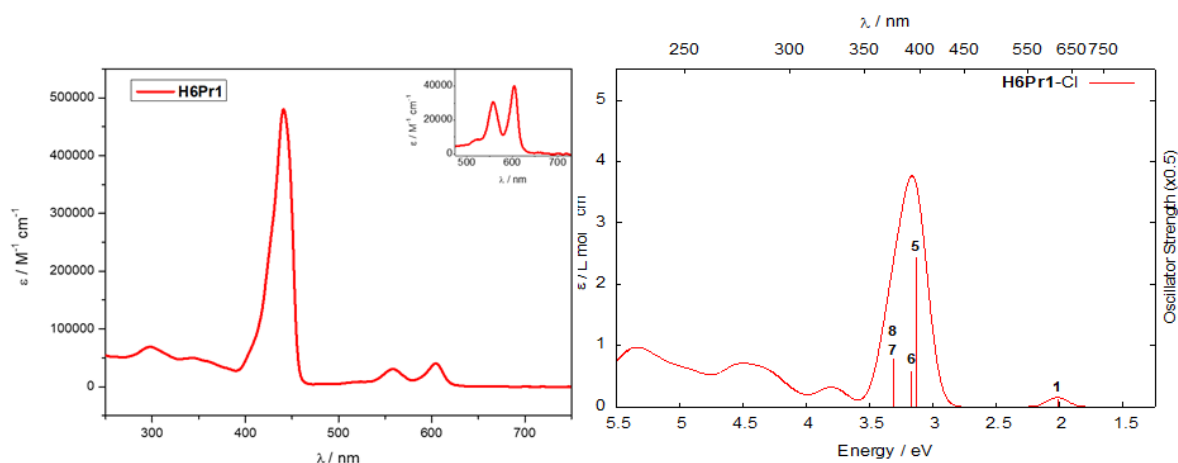
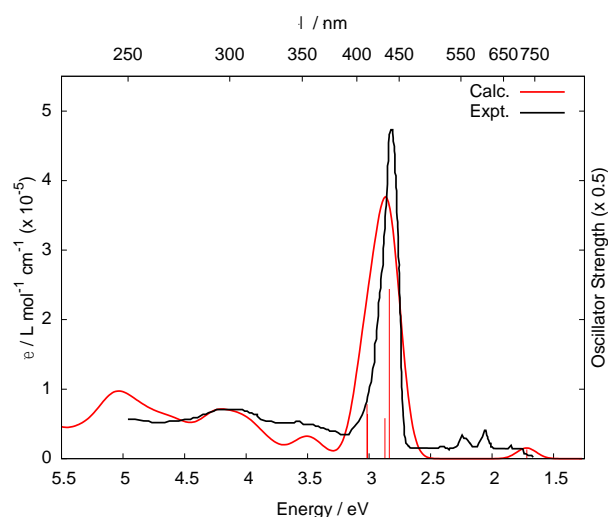


Figure S2.3. (Left) Experimental absorption spectrum for **H6Pr1**. (Right) Calculated absorption spectrum for **H6Pr1-Cl**. Selected transitions and oscillator strengths indicated as ‘stick spectra’. Predominant transitions for **H6Pr1-Cl** are numbered according to Table S2.2.



Scheme S2.1. Experimental (black) vs. calculated (Calc.) absorption spectra for **H6Pr1**. Selected transitions and oscillator strengths indicated as ‘stick spectra’. The computed spectrum is red-shifted by 0.3 eV and the intensities are multiplied by 10^5 .

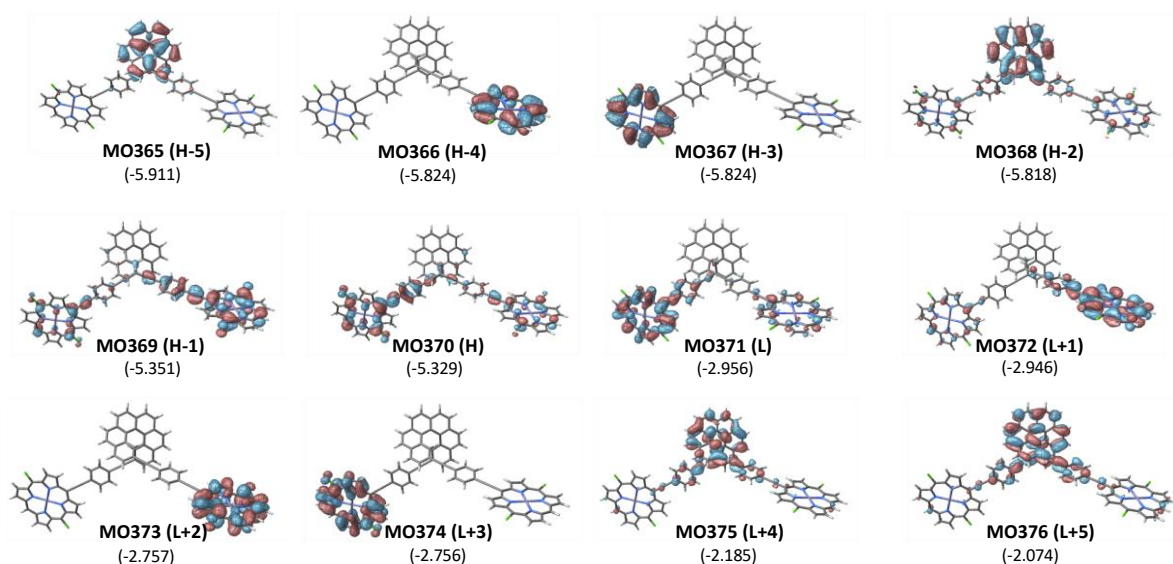


Figure S2.4. Isosurfaces (± 0.020 au) of Molecular Orbitals (MOs) involved in the selected transitions for *P-H6Pr1-Cl*. Values listed in parentheses are the corresponding orbitals energies in eV. H and L indicate the HOMO and LUMO, respectively.

Table S2.2. Selected excitations and occupied (occ)-unoccupied (unocc) MO pair contributions (greater than 6%) for *P-H6Pr1-Cl*. H and L indicate the HOMO and LUMO, respectively.

Excitation	E [eV]	λ [nm]	f	R [10^{-40} cgs]	occ. no.	unocc no.	%
#1	2.018	614	0.264	135.9	370 (H)	371 (L)	23
					367	374	14
#2	2.024	613	0.082	-108.1	369	372	19
					368	373	15
#3	2.076	597	0.001	-0.025	367	371	22
					370	374	21
#4	2.076	597	0.001	-0.143	368	372	22
					369	373	21
#5	3.136	395	4.882	2998.5	367	374	19
					370	371	10
#6	3.171	391	1.165	-2585.8	368	373	19
					367	374	10
#7	3.313	374	1.271	3980.2	367	371	24
					370	374	20
#8	3.317	374	1.569	-3885.8	368	372	24
					369	373	20
#10	3.772	329	0.182	757.9	365	376	16
#11	3.820	325	0.316	-516.4	366	376	12
					365	375	8
#13	4.172	297	0.311	122.4	365	376	6
					366	375	6
#21	4.329	286	0.143	-268.4	365	377	7
#22	4.351	285	0.422	-217.4	355	372	6
#23	4.505	275	0.279	-446.5	366	376	7

ECD Spectroscopy. The electronic circular dichroism (ECD) spectrum for **H6Pr1-Cl** is shown in Figure S2.5. The broadened computed ECD spectrum for model **H6Pr1-Cl** is in very good agreement with the experimental spectrum of **H6Pr1**, apart from the blue shift already noted (see Scheme S2.2). The following discussion is for the *P* enantiomer. In general, the transitions with large *f* also show large rotatory strengths (*R*), which are given in Table S2.2 and the text in cgs-based units of esu^2cm^2 , and the assignment of the ECD bands are in line with the absorption peaks. The assignment of the individual transitions has already been discussed in the UV-vis section and is not repeated here. The question of interest is therefore: How much of the intensity of the peak-trough pattern seen in the experimental ECD spectrum of *P*-**H6Pr1** around 450 nm is a result of exciton coupling of the Zn-porphyrin B-band transitions?

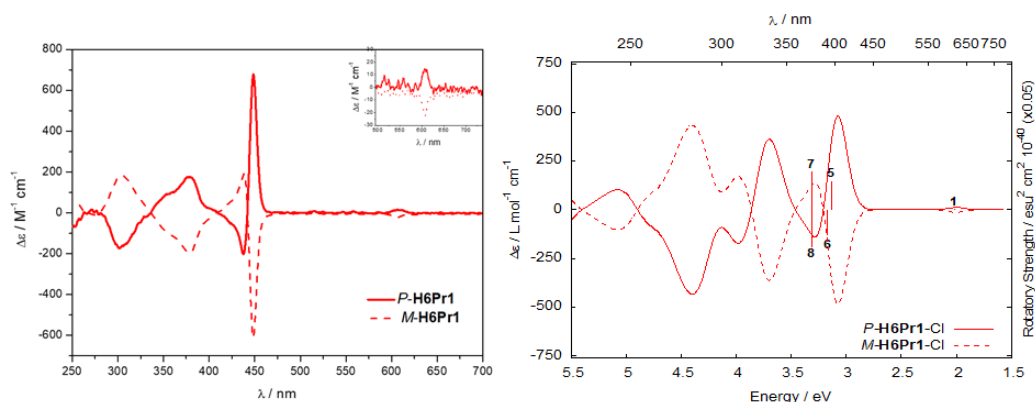
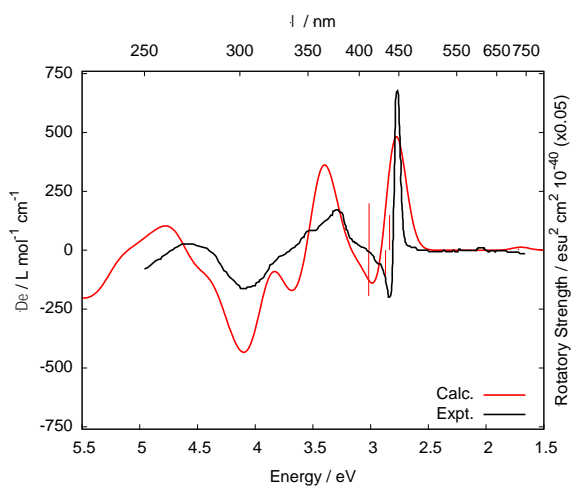


Figure S2.5. (Left) Experimental electronic circular dichroism (ECD) spectra for *P*- and *M*-**H6Pr1**. (Right) Calculated ECD spectra for *P*- and *M*-**H6Pr1-Cl**. Selected transitions and rotatory strengths for *P*-**H6Pr1-Cl** are indicated as ‘stick spectra’. Predominant transitions for *P*-**H6Pr1-Cl** are numbered according to Table S2.2.



Scheme S2.2. Experimental (black) vs. calculated (Calc.) electronic circular dichroism (ECD) spectra for *P*-**H6Pr1**. Selected transitions and rotatory strengths indicated as ‘stick spectra’. The computed spectrum is red-shifted by 0.3 eV.

To this end, calculations were performed on different dimers in the same arrangement as in the model for *P-H6Pr1*, with increasingly large parts of the center of the molecule removed, and dangling bonds capped with hydrogen. The resulting dimer structures and their adopted labels are displayed in Figure S2.6. Note that the distance between the two Zn^{2+} ions is 28.262 Å and the distance between the two carbon atoms of the porphyrins which are adjacent to the alkynyl bridge is 21.953 Å.

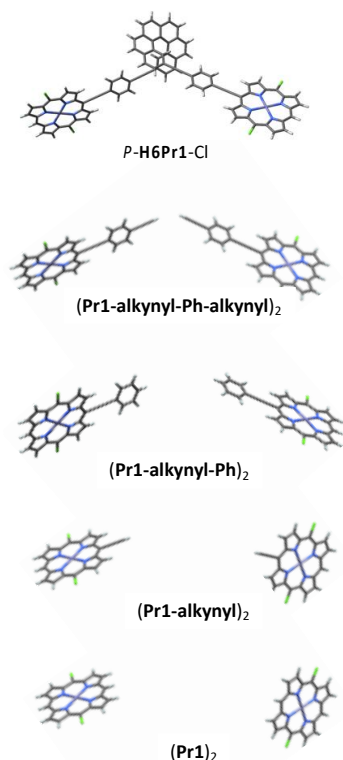


Figure S2.6. DFT-optimized structure of *P-H6Pr1-Cl* and the corresponding dimer models.

The ECD spectra of the dimer models are compared to the spectrum of the full *P-H6Pr1-Cl* system in Figure S2.7. For all dimers, frontier orbitals appear as \pm linear FFO combinations, as in the full **H6Pr1-Cl** system (Figure S2.8). When the dimer is extended from **(Pr1)₂** to **(Pr1-alkynyl-Ph-alkynyl)₂**, there happens a delocalization of the porphyrin orbitals through the linker, which we noted earlier. As seen in the calculated ECD spectra, the gradual increase of the chromophore extension in the series of models leads to the aforementioned lowering of the excitations of porphyrin B-band parentage, such that in the largest dimer, **(Pr1-alkynyl-Ph-alkynyl)₂**, the intense positive/negative pair of ECD bands (around 400 nm in the calculations) is almost aligned with those of *P-H6Pr1-Cl*. However, the presence of the helicene evidently plays a crucial role, as the intensity of the exciton CD couplet is much larger in the full system, and it is not nearly as conservative as those of the models. Moreover, some of the relevant MOs in the full system are even more extended, into the helicene, than they are in the dimer models.

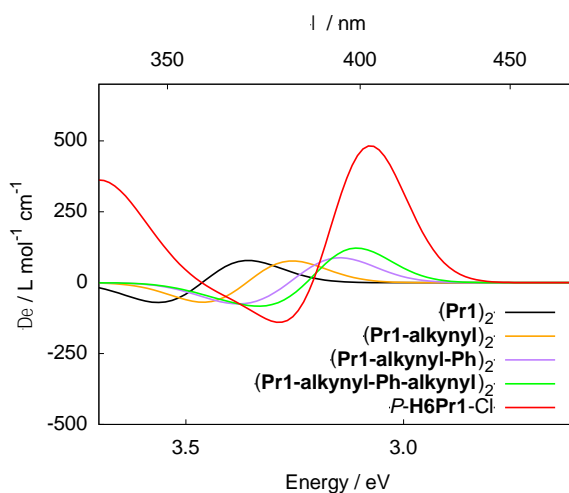


Figure S2.7. Comparison of the low energy region of the ECD spectra for *P-H6Pr1-Cl* and the corresponding dimer models of Figure S2.6.

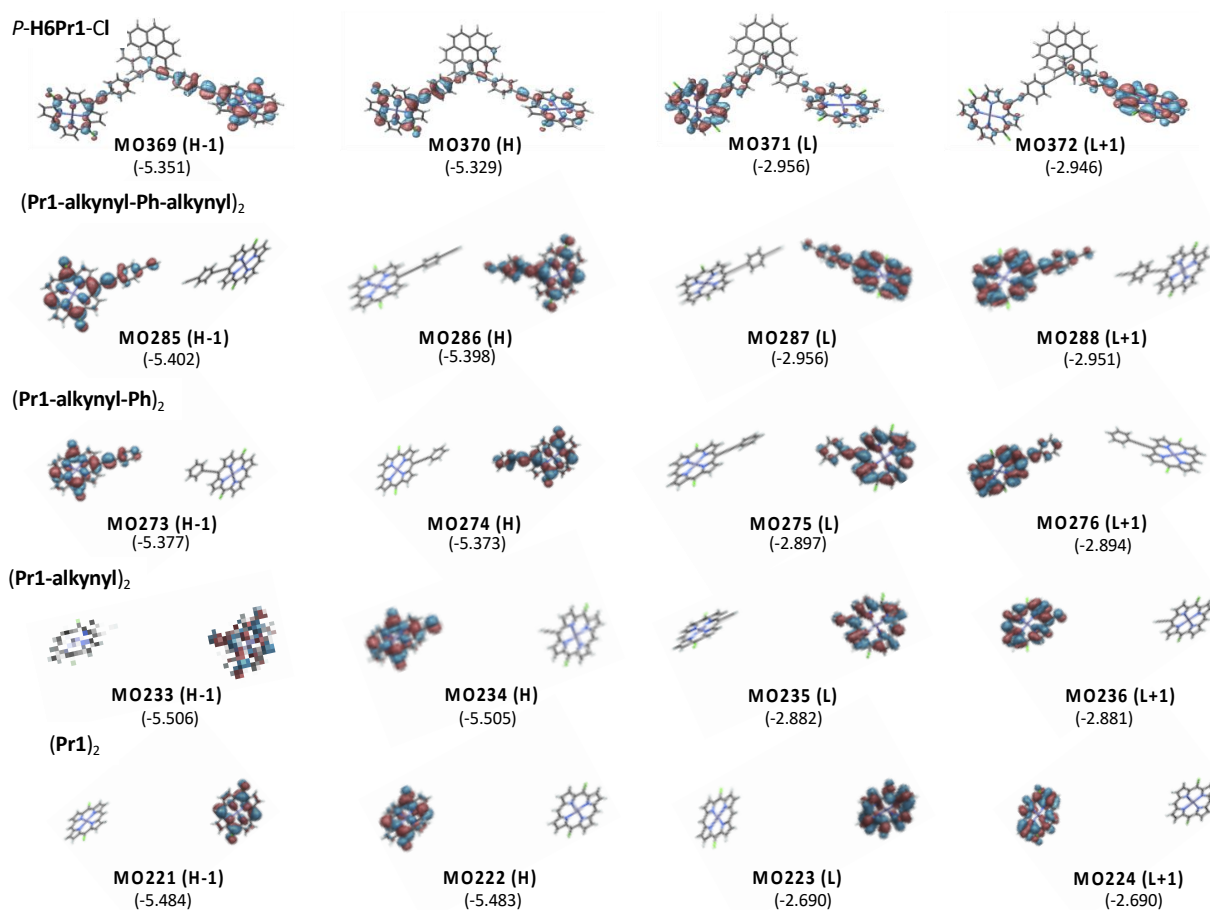


Figure S2.8. Isosurfaces (± 0.020 au) of Molecular Orbitals (MOs) involved in the selected low-energy transitions for *P-H6Pr1-Cl* and the corresponding **(Pr1-alkynyl-Ph-alkynyl)₂**, **(Pr1-alkynyl-Ph)₂**, **(Pr1-alkynyl)₂** and **(Pr1)₂** dimer models. Values listed in parentheses are the corresponding orbital energies in eV. H and L indicate the HOMO and LUMO, respectively.

Table S2.3. Selected low-energy excitations and occupied (occ)-unoccupied (unocc) MO pair contributions (greater than 14%) for *P-H6Pr1-Cl* and the corresponding (**Pr1-alkynyl-Ph-alkynyl**)₂, (**Pr1-alkynyl-Ph**)₂, (**Pr1-alkynyl**)₂ and (**Pr1**)₂ dimer models. H and L indicate the HOMO and LUMO, respectively.

Model	Excitation	E [eV]	λ [nm]	f	R [10^{-40} cgs]	occ. no.	unocc no.	%
<i>P-H6Pr1-Cl</i>	#5	3.136	395	4.882	2998.5	367	374	19
	#6	3.171	391	1.165	-2585.8	368	373	19
	#7	3.313	374	1.271	3980.2	367 370 (H)	371 (L) 374	24 20
	#8	3.317	374	1.569	-3885.8	368 369	372 373	24 20
<hr/>								
(Pr1-alkynyl-Ph-alkynyl) ₂	#5	3.188	389	4.003	1755.8	283	289	20
	#6	3.208	386	0.799	-1817.8	284	290	20
	#7	3.317	374	1.260	4871.2	283 286 (H)	287 (L) 289	25 23
	#8	3.321	373	1.645	-4767.5	284 285	288 290	25 23
<hr/>								
(Pr1-alkynyl-Ph) ₂	#5	3.218	385	3.550	1515.2	271	278	20
	#6	3.233	383	0.729	-1588.8	272	277	20
	#7	3.319	374	1.250	5201.6	271 274 (H)	275 (L) 278	25 23
	#8	3.322	373	1.663	-5107.0	272 273	276 277	25 23
<hr/>								
(Pr1-alkynyl) ₂	#5	3.337	372	2.777	1134.0	232 231	237 238	15 14
	#6	3.346	371	0.489	-1354.9	231 232	238 237	15 14
	#7	3.360	369	1.077	12175.9	231 233	235 (L) 238	18 17
	#8	3.362	369	2.034	-11937.3	232 234 (H)	236 237	18 17
<hr/>								
(Pr1) ₂	#5	3.453	359	2.422	1048.9	220 222 (H)	223 (L) 226	14 13
	#6	3.455	359	0.966	13090.9	219 221	225 224	16 13
	#7	3.456	359	2.283	-13696.3	220 222	226 223	17 14
	#8	3.459	358	0.476	425.2	219 221	224 225	14 14

For further analysis, we set up a dipole coupling model for the exciton ECD, based on the excitations of a truncated version of *P-H6Pr1-Cl* in which the [6]helicene is fully intact, but one of the Zn-porphyrins

is removed. The system is referred to by the label mono-**H6Pr1-Cl**. The ECD spectrum was calculated with the optimized structure of mono-**H6Pr1-Cl** (Figure S2.9) and can be compared to the corresponding spectra of the bi-substituted *P*-**H6Pr1-Cl** system (Figure S2.10 and Table S2.4). Figure S2.11 shows the molecular orbitals of the mono system. Clearly, its ECD spectrum bears no resemblance of that of **H6Pr1**, but it is important to point out that the chromophore does give substantial rotatory strengths in the 400 nm region (calcd.) as well.

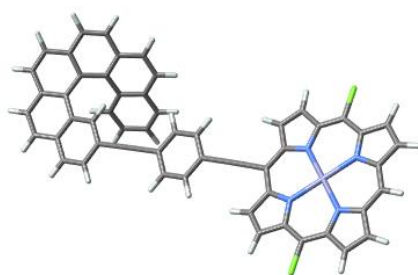


Figure S2.9. DFT-optimized structure of mono-**H6Pr1-Cl**.

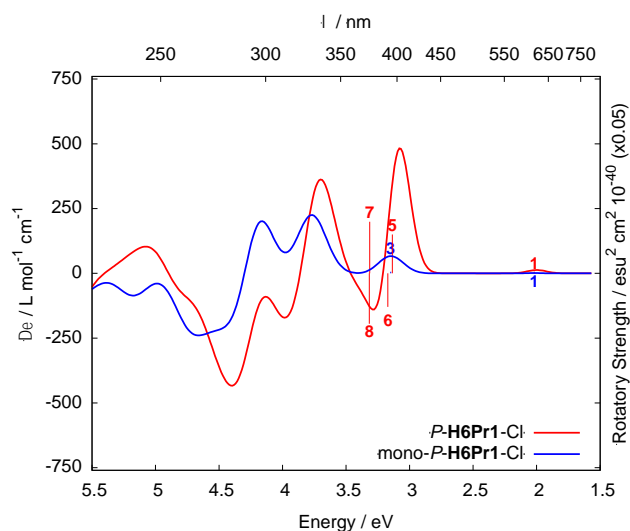


Figure S2.10. Comparison of the calculated electronic circular dichroism (ECD) spectra for the *P*-isomers of the mono- and bi-substituted **H6Pr1-Cl** compounds. Selected transitions and rotatory strengths are indicated as ‘stick spectra’. Predominant transitions for mono-*P*-**H6Pr1-Cl** are numbered according to Table S2.4.

Table S2.4. Selected excitations and occupied (occ)-unoccupied (unocc) MO pair contributions (greater than 6%) for the mono-substituted *P*-**H6Pr1**-Cl. H and L indicate the HOMO and LUMO, respectively.

Exc.	E [eV]	λ [nm]	f	R [10^{-40} cgs]	occ. no.	unocc no.	%
#1	2.018	614	0.172	2.6	228 (H)	229 (L)	31
					227	230	18
#3	3.149	394	3.027	122.0	227	230	29
					228	229	16
#4	3.313	374	1.408	-5.3	227	229	26
					228	230	23

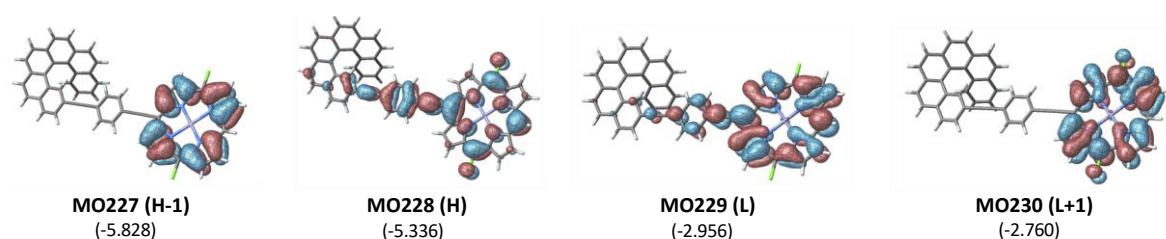


Figure S2.11. Isosurfaces (± 0.020 au) of Molecular Orbitals (MOs) involved in the selected transitions for mono-*P*-**H6Pr1**-Cl. Values listed in parentheses are the corresponding orbitals energies in eV. H and L indicate the HOMO and LUMO, respectively.

The dipole coupling model was based on a ‘matrix method’ (MM) setup as described in Ref. 19¹⁹ and 20²⁰. First, it was verified that the MM reproduced correctly the ECD spectrum of the (**Pr1**)₂ dimer in Figure S2.12. Next, electric transition dipole moment (TDM) vectors and energies of excitations #3 and #4 of mono-**H6Pr1**-Cl were used as input. The TDM vectors for these two excitations were centered at the porphyrin carbon atom adjacent to the alkynyl group. The coordinate origin was chosen to be the centroid of the six carbon atoms surrounding the helicene center on the inside perimeter of the helicene. A second set of transition dipole moment vectors centered at the opposite end of the helicene was produced by a 180° rotation around the C_2 symmetry axis of the helicene. Figure S2.13 displays the corresponding input electric TDMs and the rotated set. The calculated angle between the electric transition dipole and its magnetic counterpart for the resulting four coupled transitions are 116.4, 0, 49.7 and 180 degrees and, the corresponding calculated rotatory strengths are $-2243 \cdot 10^{-40}$ cgs, $2234 \cdot 10^{-40}$ cgs, $9428 \cdot 10^{-40}$ cgs and $-9419 \cdot 10^{-40}$ cgs. For comparison, the electric and magnetic transition dipole moments for excitations #5, #6, #7 and #8 for *P*-**H6Pr1**-Cl are shown in Figure S2.14. While the agreement is only qualitatively correct for the first coupled pair, and poor for the second, the overall magnitude of the rotatory strengths of the first two excitations is correctly reproduced, compared to those of the full system in Table S2.2. (In the MM there was very weak coupling for the second set of excitations,

resulting in basically degenerate coupled excitations whose rotatory strengths cancel). The sign of the exciton couplet is determined by the sense of the helical arrangement of the coupled TDMs, opposite for *P*- and *M*-structures^{21,22,1}. For *P*-stereoisomer, the exciton coupling signature is positive.

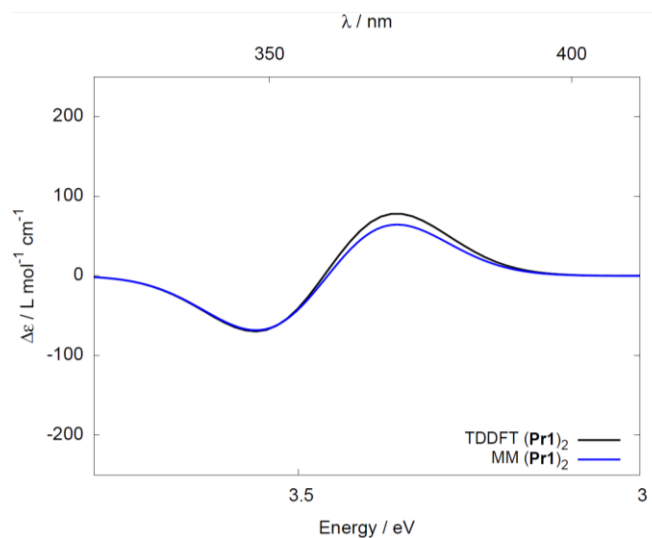


Figure S2.12. Comparison of the low-energy region of the ECD spectra of **(Pr1)₂** from a TDDFT calculation and from the matrix method (MM) dipole-coupling model. MM dipole-coupling model based on excitations #5 and #7 of **(Pr1)₂**. The TDM vectors for these two excitations were centered at the Zn²⁺ ions.

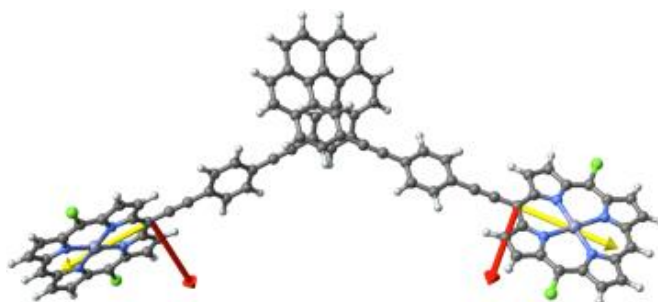


Figure S2.13. Set-up of electric transition dipole moment (TDM) vectors based on excitations #3 (yellow) and #4 (red) of mono-*P*-**H6Pr1-Cl** for exciton coupling ‘matrix method’ model for *P*-**H6Pr1-Cl**, and the rotated set of TDMs, shown together with the full structure of *P*-**H6Pr1-Cl**.

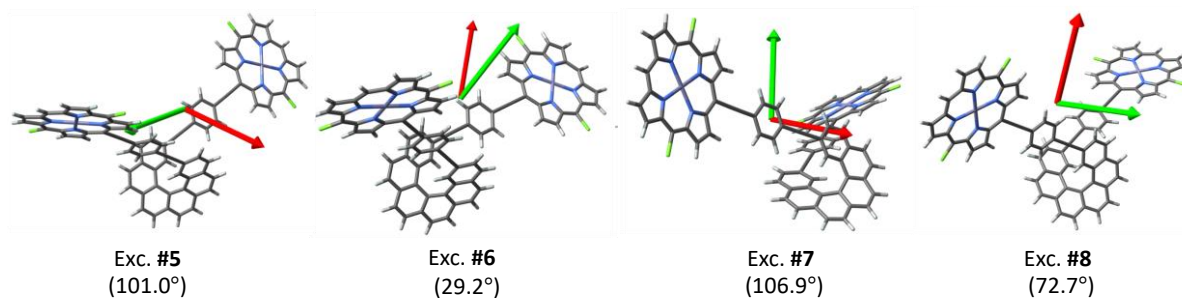


Figure S2.14. Electric (green) and magnetic (red) dipole moment vectors corresponding to excitations #5, #6, #7 and #8 for *P*-**H6Pr1-Cl** at the S_0 geometry.

The resulting MM spectrum is compared to the TDDFT-calculated spectra of mono-**H6Pr1-Cl** and **H6Pr1-Cl** (Figure S2.15). The MM exciton couplet is conservative. The peak-trough energetic separation in the broadened MM spectrum, as in the TDDFT calculation of the full system, is caused by the very large rotatory strengths and the chosen broadening, and does not reflect the actual weak splitting of the coupled excitations. The rotatory strengths, and the energetic splitting, are sensitive to the spatial separation of the origins where the un-coupled TDMs are placed. Our choice, close to the linker instead of in the porphyrin centers, is motivated by the fact that some of the MOs participating in the transitions are strongly delocalized over the linker and into the helicene. The appearance of the **H6Pr1** ECD spectrum can then be conceptualized by the exciton coupling between Zn-Pr-linker centered monomer TDMs, which is strongly perturbed by the presence of the helicene, leading to the actual non-conservative appearance of the couplet. It is also likely that the MM underestimated the contributions from the coupling of the second set of excitations of the monomer model.

A visual comparison of the simulated ECD spectrum for mono-**H6Pr1-Cl** reflects similar features as the corresponding experimental spectrum of **H6Pr2**, after the blue-shift already noted in the calculations (Figure S2.16). For mono-**H6Pr1-Cl**, the calculated ECD band at 390 nm is much weaker than for **H6Pr1-Cl** and also appears slightly blue-shifted in comparison to the bi-substituted system. Noteworthy, the weak negative band at 374 nm for **H6Pr1-Cl** does not appear for the mono-substituted system. The rotatory strengths for excitations #3 and #4 are extremely low compared to the ones for excitations #5 to #8 of **H6Pr1-Cl**.

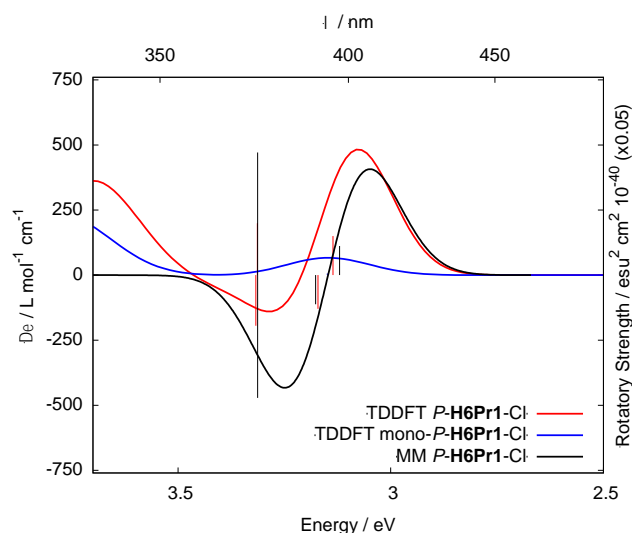


Figure S2.15. Comparison of the low-energy regions of the ECD spectra of the mono-*P*-**H6Pr1-Cl** and *P*-**H6Pr1-Cl** from TDDFT calculations and from the matrix method (MM) dipole-coupling model. MM dipole-coupling model based on excitations #3 and #4 of mono-*P*-**H6Pr1-Cl**. Selected transitions and rotatory strengths are indicated as ‘stick spectra’.

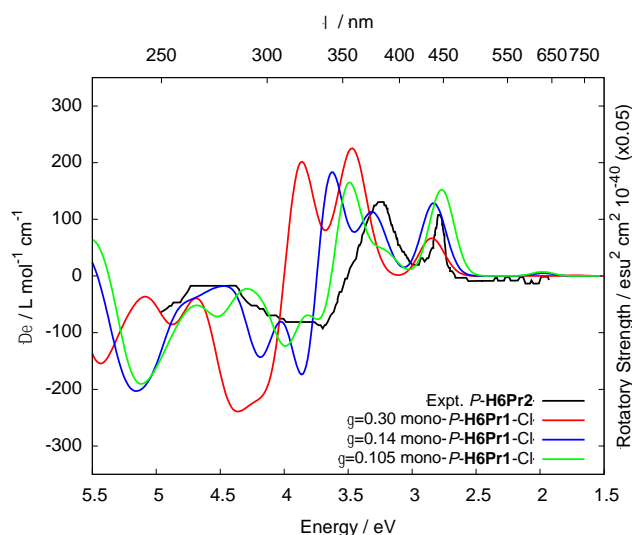


Figure S2.16. Experimental electronic circular dichroism (ECD) spectrum for *P*-**H6Pr2** and calculated ECD spectra of mono-*P*-**H6Pr1-Cl** with different values of separation parameter (γ) in the LC-PBE0 functional. The simulated ECD spectrum for $\gamma=0.3$ is red-shifted by 0.3 eV, while for $\gamma=0.14$ and 0.105, the spectra are red-shifted by 0.15 eV.

Additional Information

Absorption and ECD calculations were also performed on the optimized structure of Zn-porphyrin (Figure S2.17) and were compared with the **H6Pr1-Cl** and mono-**H6Pr1-Cl** systems (Figure S2.18).

For the UV-vis spectra, the frontier molecular orbitals of mono-**H6Pr1-Cl** and porphyrin (Figure S2.11 and Figure S2.19) are involved in the strong transition at 394 and 358 nm, respectively, which is caused by excitations #3 and #4 for both compounds. The associated transitions in the longest-wavelength of the spectra are gathered in Table S2.5. For porphyrin, the strong band is assigned to $\pi \rightarrow \pi^*$ excitations,

whereas for mono-**H6Pr1-Cl**, it also includes porphyrin to porphyrin-CC-Ph-CC intramolecular charge transfers.

The **H6Pr1-Cl** and mono-**H6Pr1-Cl** present the strongest band at 395 nm and the molar extinction coefficient for **H6Pr1-Cl** is twice the one for the mono-**H6Pr1-Cl**, indicating that the molar extinction coefficients are proportional to the number of porphyrin substituents within the molecule. Although the most intense absorption band of the porphyrin shows similar intensities as the mono-substituted system, it appears blue shifted compared to both models.

Note that the **H6Pr1-Cl** and mono-**H6Pr1-Cl** have almost identical orbital energies for the HOMO and LUMO, the HOMO-LUMO gap of the porphyrin increases as compared to them (2.79 eV for porphyrin vs. 2.37 eV for **H6Pr1-Cl**).

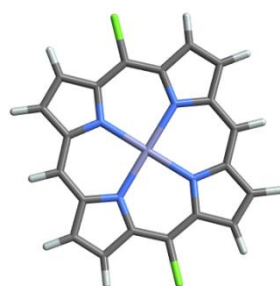


Figure S2.17. DFT-optimized structure of Zn-porphyrin.

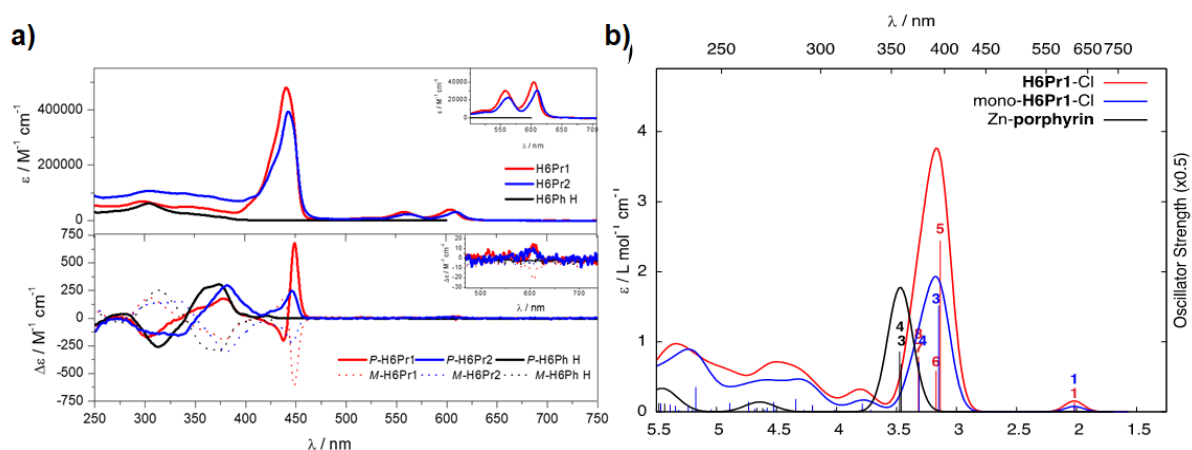


Figure S2.18. a) Experimental absorption and electronic circular dichroism (ECD) spectra. b) Calculated absorption spectra for **H6Pr1-Cl**, mono-**H6Pr1-Cl** and Zn-porphyrin. Selected transitions and oscillator strengths are indicated as ‘stick spectra’. Predominant transitions are numbered according to Table S2.5.

Table S2.5. Selected excitations and occupied (occ)-unoccupied (unocc) MO pair contributions (greater than 6%) for the mono- and bi-substituted *P*-**H6Pr1**-Cl and the porphyrin. H and L indicate the HOMO and LUMO, respectively.

Model	Exc.	E [eV]	λ [nm]	f	R [10^{-40} cgs]	occ. no.	unocc no.	%
<i>P</i> - H6Pr1 -Cl	#1	2.018	614	0.264	135.9	370 (H)	371 (L)	23
						367	374	14
	#5	3.136	395	4.882	2998.5	367	374	19
						370	371	10
	#6	3.171	391	1.165	-2585.8	368	373	19
						367	374	10
	#7	3.313	374	1.271	3980.2	367	371	24
						370	374	20
#8	3.317	374	1.569	-3885.8	368	372	24	
					369	373	20	
<hr/>								
mono- <i>P</i> - H6Pr1 -Cl	#1	2.018	614	0.172	2.6	228 (H)	229 (L)	31
						227	230	18
	#3	3.149	394	3.027	122.0	227	230	29
						228	229	16
	#4	3.313	374	1.408	-5.3	227	229	26
						228	230	23
<hr/>								
Porphyrin	#3	3.462	358	1.354	0.232	111 (H)	113	26
						110	112 (L)	25
	#4	3.475	357	1.715	-0.209	110	113	29
						111	112	22

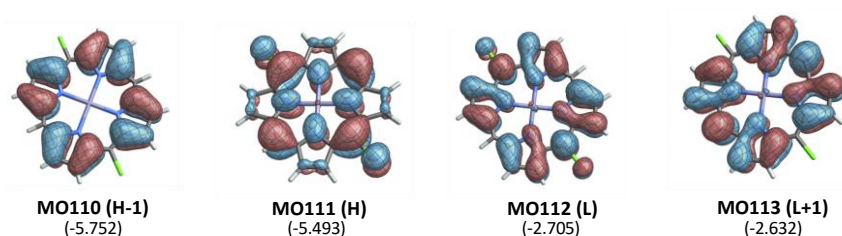


Figure S2.19. Isosurfaces (± 0.020 au) of Molecular Orbitals (MOs) involved in the selected transitions for the Zn-porphyrin. Values listed in parentheses are the corresponding orbitals energies in eV. H and L indicate the HOMO and LUMO, respectively.

Table S2.6. Calculated energies and oscillator strengths for the Q, B, and N transitions of Zn-porphyrin.

Band	E [eV]	Wavelength [nm]	f
Q _x	2.145	578	0.008
Q _y	2.156	575	0.005
B _x	3.462	358	1.354
B _y	3.475	357	1.715
N _x	4.249	292	0.000
N _y	4.313	288	0.000

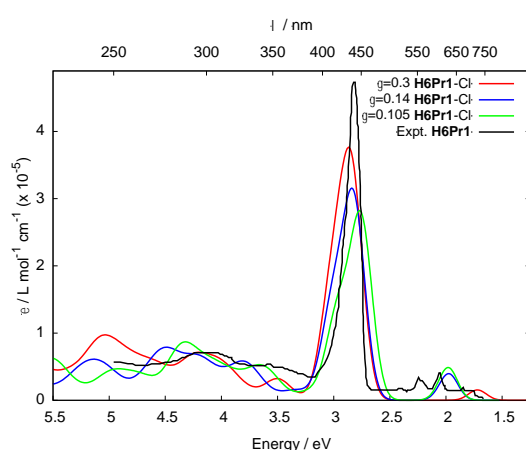


Figure S2.20. Experimental vs. calculated absorption spectra for **H6Pr1-Cl** using different separation parameter (γ) values. The simulated absorption spectrum for $\gamma=0.3$ is red-shifted by 0.3 eV, while for $\gamma=0.14$ and 0.105, the spectra are red-shifted by 0.15 eV. The intensities of all calculated spectra are multiplied by 10^5 .

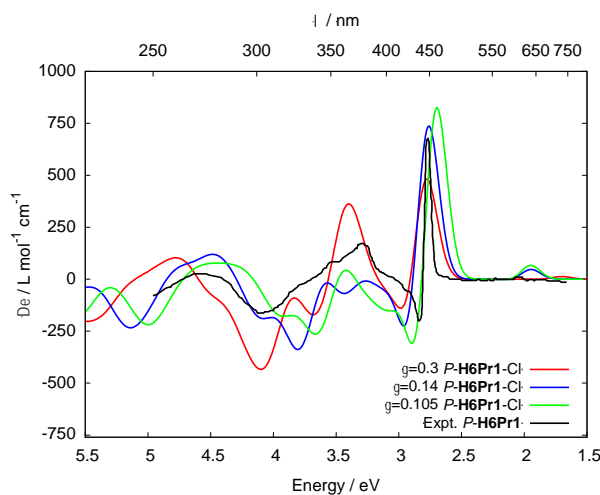


Figure S2.21. Experimental vs. calculated electronic circular dichroism (ECD) spectra for **H6Pr1-Cl** using different separation parameter (γ) values. The simulated ECD spectrum for $\gamma=0.3$ is red-shifted by 0.3 eV, while for $\gamma=0.14$ and 0.105, the spectra are red-shifted by 0.15 eV.

IV. References

- (1) N. Berova; L. D. Bari; G. Pescitelli. *Chem. Soc. Rev.* **2007**, *36*, 914-931.
- (2) Y.-C. Chang; C.-L. Wang; T.-Y. Pan; S.-H. Hong; C.-M. Lan; H.-H. Kuo; C.-F. Lo; H.-Y. Hsu; C.-Y. Lin; E. W.-G. Diau. *Chem. Commun.* **2011**, *47*, 8910-8912.
- (3) T. Higashino; Y. Kurumisawa; S. Nimura; H. Iiyama; H. Imahori. *Eur. J. Org. Chem.* **2018**, *2018*, 2537-2547.
- (4) E. Anger; M. Srebro; N. Vanthuyne; L. Toupet; S. Rigaut; C. Roussel; J. Autschbach; J. Crassous; R. Réau. *J. Am. Chem. Soc.* **2012**, *134*, 15628-15631.
- (5) D. Yao; X. Zhang; O. Mongin; F. Paul; C. O. Paul-Roth. *Chem. Eur. J.* **2016**, *22*, 5583-5597.
- (6) G. W. T. M. J. Frisch, H. B. Schlegel et al. "Gaussian 16, Revision B.01", Gaussian, Inc., Wallingford CT, 2016. URL: www.gaussian.com.
- (7) A. D. Becke. *J. Chem. Phys.* **1993**, *98*, 5648-5652.
- (8) F. Weigend; R. Ahlrichs. *Phys. Chem. Chem. Phys.*, **2005**, *7*, 3297-3305.
- (9) F. Weigend. *Phys. Chem. Chem. Phys.*, **2006**, *8*, 1057-1065.
- (10) G. Scalmani; M. J. Frisch. *J. Chem. Phys.* **2010**, *132*, 114110.
- (11) C. Adamo; V. Barone. *J. Chem. Phys.* **1999**, *110*, 6158-6170.
- (12) T. Yanai; D. P. Tew; N. C. Handy. *Chem. Phys. Lett.* **2004**, *393*, 51-57.
- (13) J. Autschbach; M. Srebro. *Acc. Chem. Res.* **2014**, *47*, 2592-2602.
- (14) B. Moore II; J. Autschbach. *ChemistryOpen*. **2012**, *1*, 184-194.
- (15) M. Srebro; J. Autschbach. *J. Chem. Theory Comput.* **2012**, *8*, 245-256.
- (16) M. Srebro-Hooper; J. Autschbach. *Annu. Rev. Phys. Chem.* **2017**, *68*, 399-420.
- (17) J. Autschbach; L. Nitsch-Velasquez; M. Rudolph In *Electronic and Magnetic Properties of Chiral Molecules and Supramolecular Architectures*; Naaman, R., Beratan, D. N., Waldeck, D., Eds.; Springer Berlin Heidelberg: Berlin, Heidelberg, 2011.
- (18) M. Gouterman. *J. Phys. Chem.* **1958**, 1139-1161.
- (19) P. M. Bayley; E. B. Nielsen; J. A. Schellman. *J. Chem. Phys.* **1969**, *73*, 228-243.
- (20) M. Rudolph; J. Autschbach. *J. Phys. Chem. A.* **2011**, *115*, 2635-2649.
- (21) K. Dhbaibi; L. Favereau; M. Srebro-Hooper; M. Jean; N. Vanthuyne; F. Zinna; B. Jamoussi; L. Di Bari; J. Autschbach; J. Crassous. *Chem. Sci.* **2018**, *9*, 735-742.
- (22) N. Harada; K. Nakanishi; N. Berova. in *Comprehensive Chiroptical Spectroscopy*, John Wiley & Sons, Inc., **2012**, *2*, 115-166.